Precise CRISPR-Cas9 gene repair in autologous memory T cells to treat familial hemophagocytic lymphohistiocytosis

Li X., Wirtz T., Weber T., Lebedin M., Lowenstein E.D., Sommermann T., Zach A., Yasuda T., de la Rosa K., Chu V.T., Schulte J.H., Müller I., Kocks C., Rajewsky K.

Science Immunology
2024 FEB ; 09(92): eadi0042
2024 FEB 02 (first published online: final publication)
doi: 10.1126/sciimmunol.adi0042

Publisher: American Association for the Advancement of Science (AAAS)

Title: Precise CRISPR-Cas9 gene repair in autologous memory T cells to treat familial hemophagocytic lymphohistiocytosis

Authors: Xun Li[1†], Tristan Wirtz[1‡], Timm Weber[1§], Mikhail Lebedin[2,3], Elijah D. Lowenstein[4], Thomas Sommermann[1**], Andreas Zach[1,3], Tomoharu Yasuda[1††], Kathrin de la Rosa[2,5], Van Trung Chu[1,6], Johannes H. Schulte[7‡‡], Ingo Müller[8], Christine Kocks[1,4], Klaus Rajewsky[1]*

Affiliations:

[1]Max-Delbrück-Center for Molecular Medicine in the Helmholtz Association (MDC), Immune Regulation and Cancer; 13125 Berlin, Germany.

[2]Max-Delbrück-Center for Molecular Medicine in the Helmholtz Association (MDC), Immune Mechanisms and Human Antibodies; 13125 Berlin, Germany.

[3]Charité - Universitätsmedizin Berlin, corporate member of Freie Universität Berlin and Humboldt-Universität zu Berlin; 10117 Berlin, Germany.

[4]Max-Delbrück-Center for Molecular Medicine in the Helmholtz Association (MDC), Developmental Biology/Signal Transduction; 13125 Berlin, Germany.

[5]Berlin Institute of Health (BIH) at Charité, Center of Biological Design, 13125 Berlin, Germany

[6]Max-Delbrück-Center for Molecular Medicine in the Helmholtz Association (MDC), Genome Engineering & Disease Models; 13125 Berlin, Germany.

[7]Department of Pediatric Hematology, Oncology and Stem Cell Transplantation, Charité - Universitätsmedizin Berlin, corporate member of Freie Universität Berlin, Humboldt-Universität zu Berlin, and Berlin Institute of Health (BIH); 10117 Berlin, Germany.

[8]Division of Pediatric Stem Cell Transplantation and Immunology, Clinic of Pediatric Hematology and Oncology, University Medical Center Hamburg-Eppendorf; 20246 Hamburg, Germany.

*Corresponding author. Email: klaus.rajewsky@mdc-berlin.de.

† Current address: Department of Microbiology and Immunology, University of California San Francisco (UCSF), San Francisco, CA, USA.
‡ Current address: Pfizer Inc., San Diego, CA 92121, USA.
§ Current address: Laboratory of Experimental Immunology, Institute of Virology, Faculty of Medicine and University Hospital Cologne, University of Cologne; 50931 Cologne, Germany.
** Current address: Dynamic42 GmbH; 07745 Jena, Germany.
†† Current address: Department of Immunology, Graduate School of Biomedical and Health Sciences, Hiroshima University, Hiroshima 734-8551, Japan.
‡‡ Current address: General Pediatrics, Hematology and Oncology, University Children's Hospital Tübingen; 72076 Tübingen, Germany.

Abstract:

Familial hemophagocytic lymphohistiocytosis (FHL) is an inherited, often fatal immune deficiency characterized by severe systemic hyperinflammation. Although allogeneic bone marrow transplantation can be curative, more effective therapies are urgently needed. FHL is caused by inactivating mutations in proteins that regulate cellular immunity. Here, we used an adeno-associated virus (AAV)–based CRISPR–Cas9 system with an inhibitor of non-homologous end joining (NHEJ) to repair such mutations in potentially long-lived T cells ex vivo. Repaired CD8 memory T cells efficiently cured lethal hyperinflammation in a mouse model of Epstein–Barr virus (EBV)–triggered FHL2, a subtype caused by perforin-1 (*Prf1*) deficiency. Furthermore, repair of *PRF1* and Munc13-4 (*UNC13D*)—whose deficiency causes the FHL subtype FHL3—in mutant memory T cells from two critically ill FHL patients restored T cell cytotoxicity. These results provide a starting point for the treatment of genetic T cell immune dysregulation syndromes with repaired autologous T cells.

One-Sentence Summary:

Mutant dysfunctional T cells can be repaired by CRISPR–Cas9 gene correction and used to cure lethal EBV-triggered hyperinflammation.

Main Text:

INTRODUCTION

Hemophagocytic lymphohistiocytosis (HLH) is a life-threatening hyperinflammation syndrome caused by the dysregulation and aberrant activation of cytotoxic T lymphocytes, natural killer (NK) cells, and macrophages, which leads to cytokine storms and immune cell–mediated damage of multiple organ systems (*1, 2*). The dysregulated processes by which impaired granule-mediated cytotoxicity causes hereditary or familial HLH (FHL) involve prolonged contact between lymphocytes and their target cells as well as failure to terminate the immune response by elimination of target cells, antigen-presenting cells, and cytotoxic cells (*1, 3–6*). Consequently, cytokine levels, T cell proliferation, and macrophage activation continue to escalate and multi-organ failure ultimately results (*7, 8*).

FHL manifests in early infancy, mostly in the first 6 months after birth (*4, 9*). Combinatorial immunochemotherapy is used to control the cytokine storm and dampen cellular proliferation (*10–12*). It involves cytostatic, corticosteroid, and immunosuppressant agents and is often associated with severe side effects following prolonged treatment (*2*). The median survival of pediatric patients is in the range of months unless hematopoietic stem cell transplantation (HSCT) is performed, but mortality still remains high (*2, 9–11, 13*). Incomplete remission of disease activity and graft rejection pose major risks in this vulnerable cohort of patients (*14, 15*).

Because only approximately 50% of FHL patients survive long-term overall (*11, 16*), there is an urgent clinical need to improve outcomes and treatment side effects. One possibility is to use autologous, repaired T cells as a bridge-to-transplant therapy to improve the patients' condition and further reduce the risks associated with HSCT. Repaired long-lived T memory stem (T_{SCM}) cells may also confer longer-term protection on their own, since genetically

modified T cells can survive for a decade or more (*17, 18*). T_{SCM} cells resemble naïve T (T_N) cells, are less differentiated than other memory T cell subsets, and have been proposed to reside at the top of the T cell hierarchy in a progressive model of T cell differentiation (*19*). Only T_N and T_{SCM} cells possess the ability to reconstitute the full spectrum of T memory cell subsets, including T_{SCM} cells, after allogeneic HSCT (*20*).

Most children with FHL have genetic loss-of-function mutations that affect proteins required for the normal cytotoxic functions of T cells and NK cells (*1*). Complete loss or severely compromised function of perforin-1 (PRF1) and Munc13-4 (encoded by *UNC13D*) cause FHL2 and FHL3, respectively, and combined account for about two thirds of all FHL cases (*6, 21*). PRF1 is a cytolytic effector protein, and a major component of the cytolytic granules that promote osmotic lysis of target cells, whereas Munc13-4 is required for release of lytic granule contents (*6, 22*). By contrast, most cases of adult or secondary HLH appears appear to not be genetically determined, although hypomorphic alleles in FHL loci represent predisposing factors in a fraction of adult patients, complicating an initial diagnosis of primary versus secondary HLH (*1, 9, 10*).

HLH can be triggered by any infection or malignancy, acting alone or in concert with genetic susceptibility factors, and infectious triggers vary by geographic region (*2, 4*). Herpesviruses such as Epstein–Barr virus (EBV) and cytomegalovirus are commonly associated with HLH in developed countries (*1, 4, 9*), with EBV infection being the most frequent and severe initiating event for both, primary and secondary HLH (*1, 2*). However, in many FHL cases, no infectious trigger can be identified (*23*). EBV latently infects and transforms B lymphocytes, resulting in lifelong virus reactivation episodes and malignant lymphoproliferation,

which is normally contained in healthy humans by immunosurveillance through T and NK cells, but spirals out of control under immunosuppression (*24*).

Here we demonstrate the suitability of precisely repaired autologous T cells for the treatment of FHL. We repaired perforin-1–deficient mouse memory T cells by adeno-associated virus (AAV)–templated CRISPR–Cas9–mediated gene correction and used them to cure lethal, EBV-induced hyperinflammation in a mouse model of FHL. Furthermore, T cells isolated from pediatric patients with FHL2 and FHL3 were successfully expanded and repaired, restoring CD8 T cell cytotoxicity, while retaining a T_{SCM} cell–like phenotype. Our results provide a starting point for the clinical implementation of autologous T cell therapy in FHL patients.

RESULTS

A preclinical mouse model of EBV-triggered FHL

We previously developed a genetic mouse model that recapitulates major features of fatal EBV-triggered FHL2 in humans (*25*). In this model, the EBV oncoprotein latent membrane protein 1 (LMP1) or LMP1 together with LMP2A (LMP1/2A) is expressed in a small fraction of mouse B cells in an inducible manner, mimicking human EBV infection. When combined with a genetic perforin-1 deficiency (*26*), inducible EBV LMP1 or LMP1/2A expression is sufficient to cause a fulminant hyperinflammatory syndrome (*25*). Within days after induction of LMP1 or LMP1/2A expression in B cells, mice succumbed to acute lymphoproliferative disease (Fig. 1A), which manifested as spleen enlargement and white blood cell infiltration in liver, thrombocytopenia, and elevated serum markers indicating widespread tissue damage (Fig. 1, B to D). This mouse model allowed us to explore gene therapy approaches that may prevent, mitigate, or cure HLH-like disease through the transfer of autologous, gene-corrected T cells.

A highly efficient gene repair strategy for primary T cells

We first established an ex vivo gene repair strategy in primary mouse T cells (Fig. 2A). For this purpose, we used CRISPR–Cas9 to introduce a double-strand DNA break and AAV to deliver a DNA donor template for homology-directed repair (HDR) and combined this approach with an inhibitor of non-homologous end joining (NHEJ) (*27*). Ribonucleoprotein particles (RNPs) composed of Cas9–sgRNA complexes were electroporated into cells (*28*) followed by repair template delivery through infection with AAV-DJ (*29*), an engineered derivative of AAV-2 with tropism for mouse cells (*30*). Sixteen hours of exposure to the DNA-dependent protein kinase catalytic subunit (DNA-PKcs) inhibitor M3814 at 5 μM (*27, 31*)—a concentration well tolerated in patients when given for weeks (*32*)—increased HDR events by about twofold in two mouse loci: wildtype *B2m* (fig. S1, A and B) and mutated *Prf1* (Fig. 2, B and C), reaching high knock-in repair efficiencies of greater than 50% as measured by mCherry reporter expression (table S1). Our results are in line with a recent report about high knock-in efficiency in mouse T cells using related technology (*33*). Sorted, repaired $CD8^+mCherry^+$ T cells expressed *Prf1* in response to activation, whereas mock-repaired T cells carrying a stop codon in exon 3 showed similar knock-in efficiencies, but did not express *Prf1* (Fig. 2, C and D). Sequencing of the targeted alleles confirmed a high frequency of precise HDR events (Fig. 2E; fig. S1C; and table S2). Thus, our strategy enables efficient repair of *Prf1* mutations in mouse primary T cells.

Efficient gene repair of potentially long-lived memory T cells

Antigen-experienced, potentially long-lived memory T cells are a preferred source of T cells for T cell therapies (*19*) and are present in the blood of patients suffering from primary and

secondary HLH (*7, 8, 34, 35*). Specifically, less differentiated, $CD62L^+$ T cell subsets such as central effector memory T (T_{CM}) cells possess superior immune reconstitution, self-renewal, and persistence ability in vivo to $CD62L^-$ effector memory T (T_{EM}) cells (*19, 36*). We tried to induce such cells in our EBV–*Prf1*-deficiency FHL2 mouse model by titrating down the inducer of LMP gene induction (tamoxifen), thus generating fewer LMP-expressing B cells, resulting in sublethal lymphoproliferation and absence of overt disease (Fig. 3A). These conditions allowed us to isolate $CD8^+CD44^{hi}$ T cells with T_{CM} and T_{EM} cell phenotypes around 28 days after LMP induction when antigen-specific, terminally differentiated T effector cells had largely disappeared (Fig. 3B). This memory T cell population contained antigen-specific T cells that showed strong proliferative capacity upon exposure to LMP1-expressing B cells (Fig. 3C). The memory T cells could be expanded to sufficiently high numbers to be successfully gene-repaired ex vivo (using the strategy shown in Fig. 1A), with more than 50% mCherry-reporter knock-in efficiency (Fig. 3D). When further expanded and sorted, repaired $CD8^+$ memory T cells were found to express PRF1 (Fig. 3E) and to possess pronounced killing activity towards LMP1-expressing B cells (Fig. 3F). As predicted, mock-repaired $CD8^+$ memory T cells (carrying a stop codon in exon 3) failed to express PRF1, and had a lower killing activity (Fig. 3, D to F). We are thus able to genetically repair *Prf1*-mutant $CD8^+$ memory T cells and restore their cytotoxic activity.

Prevention and cure of HLH-like disease in mice by repaired memory T cells

With readily expandable, *Prf1*-repaired memory T cells in hand, we were able to test their potential to contain otherwise fatal HLH-like disease (REF Tristan) (Fig. 4A). We adoptively transferred 1×10^6 repaired or mock-repaired memory T cells into *Prf1*-deficient *Cd19*-

Cre^{ERT2};LMP^{flSTOP} mice, either 1 day before, or 1 to 2 days after, LMP-induction. Recipient mice were neither pre-conditioned nor lymphodepleted. In both scenarios, repaired T cells fully controlled LMP-driven, pathogenic B cell proliferation, and protected and rescued mice from HLH-like disease, whereas mock-repaired T cells failed to do so (Fig. 4, B to D). These experiments establish gene repaired autologous T cells as a promising therapeutic approach for human FHL in a preclinical model.

Efficient gene repair in mutant T cells from FHL patients

To explore the feasibility of gene repair in mutant T cells from FHL patients, we obtained T cells from two pediatric patients in remission after immunochemotherapy. One child suffered from FHL2 (*PRF1* deficiency) and the other from FHL3 (Munc13-4/*UNC13D* deficiency). As is typically the case, blood samples from these patients were precious and only contained a limited number of cells. Therefore, we first expanded the patients' T cells using a protocol that supports expansion of T_{SCM} cells from the naïve T cell pool with a combination of IL-7 and IL-15 (*19, 37, 38*). We then assessed targeted mutagenesis in these expanded, blood-derived T cells by inserting an mCherry reporter into the *B2M* locus (fig. S2, A and B). RNPs were electroporated into the cells, followed by infection with AAV6 for donor repair template delivery (*39*). With T cells from both patients, we achieved consistently high (>80%) knock-in efficiencies, as measured by mCherry reporter expression (fig. S2C and table S1), as well as a high frequency (>70%) of HDR targeting events, as determined by sequencing (fig. S2D).

Restoring patient CD8 T cell cytotoxicity by correcting *PRF1* mutations in exon 3

For gene repair of mutated *PRF1* and *UNC13D* genes, blood-derived patient T cells were expanded with IL-7 and IL-15, aliquoted, frozen, and aliquots thawed, targeted and analyzed (Fig. 5A). The FHL2 patient carried two different recessive mutations in exon 3 of *PRF1*: (i) a three-nucleotide deletion leading to an in-frame deletion of lysine 285 (c.853-855del AAG(285delK)) on one allele and (ii) a c.1349C>T(T450M) missense mutation leading to the exchange of threonine to methionine on the other (Fig. 5B). We devised two gene correction strategies (Fig. 5B). In the first, we replaced the mutated versions of exon 3 with a repaired version (table S3). Inspired by a recent strategy for pan-mutation correction (*40*), we also tried a second approach, replacing exon 3 by a full-length *PRF1* cDNA preceded by a sequence encoding a T2A self-cleaving peptide (table S4). This second strategy places the perforin-1 cDNA under endogenous transcriptional and translational control and allows for pan-gene correction of the ~60 known pathogenic *PRF1* mutations (*6, 41, 42*), with the exception of frameshift or nonsense mutations in exon 2.

Since patient cells were limiting, we used T cells from three healthy donors to assess cell viability during gene editing and expansion post-editing, as well as functional performance (Fig. 5, C to F). T cells that underwent gene repair (RNP/AAV6) expanded as well as cells that received Cas9–sgRNA complexes in the absence of AAV6 (RNP), the latter causing *PRF1* knock-outs (Fig. 5C), both yielding 8-9×10^5 edited T cells after 6 days (starting from 10^5 T cells). Addition of NHEJ inhibitor M3814 lead to a 30 to 40% reduction of cell yields consistent with its known effect on cell viability (*27, 31*). The two *PRF1* gene targeting strategies both achieved efficient gene correction with a high fraction of perforin-1–expressing cells, which was increased by about twofold in the presence of the NHEJ inhibitor M3814 (i.e, from 25% to 60%) (Fig. 5D and table S1). We next measured the expression of intracellular perforin protein levels

in targeted and non-targeted T cells in response to activation. Perforin-1 expression in repaired T cells nearly reached wild-type levels seen for non-targeted T cells (Fig. 5E). In cells repaired with strategy 1 (*PRF1* exon 3 replacement), perforin-1 expression was slightly higher than in cells repaired with strategy 2 (*PRF1* cDNA knock-in). Most of the perforin-1 expression was observed in CD8 T cells (fig. S3). We assessed the cytotoxic activity of the repaired T cell populations towards human B lymphoma cells in a T cell killing assay, using a CD19–CD3 bispecific T cell engager (BiTE) antibody (*43*) (Fig. 5F). Both repair strategies 1 and 2 restored cytotoxic activity as compared to the null alleles (knock-out). In this assay, the cytotoxic activity measured was influenced by the fraction of cells expressing perforin-1 and only around 60% of T cells in the repaired T cell populations expressed perforin as compared to 100% in the non-targeted control cells.

Encouraged by these results, we attempted gene repair in FHL2 patient T cells. As the c.1349C>T(T450M) missense mutation is known to generate an altered perforin precursor with impaired proteolytic maturation (*44*), perforin expression was detectable in CD8 T cells from this patient (Fig. 6A). In the absence of AAV6 DNA repair template donor (RNP/M3814), targeting of perforin-1 led to the generation of null alleles, abolishing perforin-1 expression (Fig. 6A). With both gene targeting strategies (Fig. 5B), we achieved efficient and reproducible gene correction in the presence of AAV6 repair templates and NHEJ inhibitor M3814 with a high fraction perforin expressing cells (Fig. 6A and table S1) owing to a high frequency of HDR targeting events (~60% and ~40%, respectively) (Fig. 6B). Use of only one sgRNA (*sgPRF1.2*) instead of two led to a somewhat reduced, but still high level of targeting with around 50% of perforin-1–expressing T cells (table S1). The repaired CD8 T cells showed strongly improved cytotoxic activity towards human B lymphoma cells (Fig. 6C and fig. S4). Importantly, flow

cytometry phenotyping of the repaired T cells 6 days after CRISPR–Cas9 gene repair indicated that they predominantly had a CD45RA$^+$CD62L$^+$CD95$^+$ T_{SCM} cell–like phenotype—distinguishing them from CD45RA$^+$CD62L$^+$CD95$^-$ T_N cells (*19, 38*)—and did not overexpress T cell exhaustion markers (*45–47*) (Fig. 6, D and E, and fig. S5).

In order to assess the specificity of the sgRNAs used, we employed GUIDE-seq (genome-wide unbiased identification of double-strand breaks enabled by sequencing) (*48*). GUIDE-seq detects the integration of double-stranded oligodeoxynucleotide (dsODN) tags into sites of nuclease-induced DNA double-strand breaks by amplification of tag-containing genomic DNA followed by deep sequencing (*49, 50*). Since integration of dsODN tags at sites of DNA double-strand breaks appears to be dependent on NHEJ (*49*), we used both untreated patient T cells and patient T cells treated with the NHEJ inhibitor M3814 (fig. S6A). As expected, we detected a higher frequency of dsODN integrations in untreated T cells compared to M3814-treated T cells (fig. S6B). However, the majority of GUIDE-seq reads for both sgRNAs mapped to the intended on-target sites. A major off-target site was observed for the sgRNA targeting site 1 in *PRF1* (fig. S6B), but this was located in an intergenic region, and was therefore unlikely to cause pathogenic mutations. Taken together, we established a strategy that allows efficient *PRF1* gene repair in patient T cells, restoring the cytotoxic activity of repaired CD8$^+$ T cells.

Restoring T cell cytotoxic activity by correcting an allele-specific mutation in *UNC13D*

The FHL3 patient carried two different recessive mutations in *UNC13D* leading to premature stop codons: (i) a four-nucleotide deletion frameshift mutation in exon 24 on one allele and (ii) a c.766 C>T(p.R256X) nonsense mutation in exon 10 on the other. In order to restore cytotoxic activity in T cells from this patient, we attempted allele-specific gene correction. To this end, we

took advantage of a PAM site downstream of the of c.766C>T exchange in exon 10 and designed an sgRNA that specifically targets this mutant allele to replace the mutated exon 10 with a repaired version (Fig. 7A and table S5). This strategy restored degranulation capacity in about 40% of the repaired patient T cells (Fig. 7B) and about one third of targeted alleles underwent HDR events (Fig. 7C). This was sufficient to restore efficient cytotoxic activity in the repaired patient T cells (Fig. 7D and fig. S7). Similar to the repaired T cells from the FHL2 patient, 6 days after CRISPR–Cas9 treatment, the vast majority of the repaired CD8 T cells from the FHL3 patient had a $CD45RA^+CD62L^+CD95^+$ T_{SCM} cell–like phenotype (*19*) and were negative for the T cell exhaustion markers PD1 and TIGIT (*45*) (Fig. 7, E and F, and fig. S5). Off-target analysis by GUIDE-seq for the sgRNA targeting *UNC13D* indicated one major off-target site in a gene important for TNFα-mediated apoptosis (*BRI3*), suggesting that for clinical applications this particular sgRNA is not suitable (fig. S6). Nevertheless, our results demonstrate the feasibility of efficient allele-specific gene correction for *UNC13D*-mutated T cells from FHL3 patients. These results thus extend our repair strategy to a second genetic locus whose mutation causes HLH disease in humans.

DISCUSSION

Our study provides proof-of-principle that precisely repaired memory T cells can not only prevent, but indeed cure FHL2-like disease in mice in vivo. Although we cannot exclude that other T cell subsets could be used as well for this purpose, our results nevertheless are in line with recent evidence that adoptive, virus-specific T memory cell therapy can cure mice from active, EBV-triggered FHL2 and 3 (*51*). Precise gene repair reduces many of the safety concerns associated with lentiviral vectors, such as insertional mutagenesis near oncogene and tumor

suppressor loci, and ectopic or otherwise deregulated gene expression (*52–54*). These results therefore suggest that precisely repaired T cells may be a useful bridging therapy for acutely ill HLH patients, stabilizing these patients until curative treatment by HSCT or even replacing HSCT altogether. We consequently proceeded to develop CRISPR–Cas9–AAV6–based gene correction strategies in human T cells to correct mutations in *PRF1* and *UNC13D*, which together account for more than half of FHL cases (*6, 21*).

For the FHL2 gene *PFR1*, we provide two "off-the-shelf" gene repair strategies that cover mutations in exons 2 and 3, which encode the 555 amino acids of the perforin polypeptide (*6*). One strategy replaces the larger exon 3, covering about two thirds of the known disease mutations (*42*). We also provide a "universal" cDNA insertion strategy that additionally covers mutations in exon 2 (except frameshift and nonsense mutations), by placing an expression-optimized *PRF1* open reading frame under endogenous locus control. Both strategies worked well, although the pan-mutation correction approach was slightly less efficient (tables S1 and S2).

For the FHL3 locus *UNC13D*, which spans 32 exons and encodes the 1090 amino acid polypeptide Munc13-4, we used allele-specific gene repair, taking advantage of a PAM site downstream of the patients' mutation in exon 10. Since the other FHL3 mutation of this patient affected exon 24, this generated a genetically heterozygous "carrier state" with one functional (repaired) and one null allele. Nevertheless, we achieved full restoration of cytotoxic activity in the repaired T cells (Fig. 7 and fig. S4). Although a "universal" cDNA repair strategy remains challenging for large cDNAs such as *UNC13D*, it is feasible for the smaller FHL4 and FHL5 loci, *STX11* and *STXBP2*. Thus, our T cell gene repair strategies provide a toolbox that can be

applied to other rarer FHL subcategories and should also be useful for gene correction of other monogenic T cell–based primary immunodeficiencies (*55*).

The presence of M3814, a selective inhibitor which suppresses NHEJ (*27, 31*), increased HDR-mediated precise gene repair by roughly 1.5-to-2-fold (tables S1 and S2). However, even without this inhibitor, gene repair efficiencies in patient T cells in the *PRF1* and *UNC13D* loci (tables S1 and S2) may be sufficient to suppress FHL in patients, given that in mouse models FHL can be prevented by bone marrow or T cell populations containing 10 to 20% of cells with intact perforin-1 loci (*34, 56*). Similarly, in patients with primary hereditary HLH, 20 to 30% donor chimerism is protective against late reactivation of the disease more than 180 days post HSCT (*57*). A case in point is our FHL2 patient: this child underwent allogeneic bone marrow transplantation at the age of 4 months and remains disease-free despite a low donor chimerism of only 21% in the T cell compartment (Supplementary Text).

Any adoptive T cell therapy regimen is dependent on protocols that allow T cells to be expanded to sufficient numbers (*19*). Here, we successfully adapted a simple cell culture protocol that allowed us to expand and repair mutated potentially long-lived T_{SCM} cells from two critically ill pediatric FHL patients who had undergone immunochemotherapy in anticipation of HSCT. This protocol was developed for the rapid expansion of virus-specific T_{SCM} cells from a mixed naïve T–T_{SCM} cell population present in blood (*19, 38*) and employs a combination of IL-7 and IL-15 to support the development and expansion of T_{SCM} cells, respectively (*37*). The protocol relies on enrichment of cells with a T_{SCM} cell–like phenotype owing to the culture conditions and does not require any cell sorting or the need to isolate rare cells. Furthermore, T cell populations highly enriched for T_{SCM}-like cells showed high cytotoxic activity already two days after reactivation (Figs. 5F and 6C and fig. S4). Importantly, we were able to cryopreserve

and later reactivate patient T cells after the initial expansion, greatly facilitating clinical applications.

Immunosuppressive treatment is key to induce remission and prepare FHL patients for HSCT (*10, 11*). A priori, it was unclear, whether T cells from a post-hypercytokinemic and immunosuppressive environment would be amenable to precise CRISPR–Cas9–mediated gene repair and if so, how well gene correction would restore their effector function. Our study clearly established that, at least for the two FHL patients tested, these considerations may be of lesser concern. Gene-repaired T_{SCM} cells from our two FHL patients showed no signs of T cell exhaustion and could be differentiated into bona fide cytotoxic CD8 T cells with restored effector functions. These results are in line with earlier proof-of-concept studies that used lentiviral or retroviral insertion to overexpress human or mouse genes and reported restored cytotoxicity in Munc13-4– or perforin-1–deficient T cells (*34, 58–60*), tumor reduction in EBV-induced lymphoma, and prevention of lymphocytic choriomeningitis-triggered FHL2 (*34*) or FHL3 (*59*).

Our results are relevant for clinical translation because they demonstrate that T cells from pediatric patients who received etoposide, dexamethasone, and cyclosporine A treatment are suitable for precise gene repair ex vivo. In contrast to allo-HSCT, which is associated with serious risks and side effects (*14, 15*), and chimeric antigen receptor (CAR) T cell therapy, which can be used only once or twice in a given patient (*61*), autologous T cells for adoptive T cell therapy can be regarded more like a drug that can be given repeatedly. Indeed, adoptive cell therapy with virus-specific T cells is well tolerated, has proven highly effective in immunocompromised patients with EBV and CMV infections, and can even be used prophylactically (*62*). To avoid the challenges related to the cost and complexity of AAV

production, our gene targeting strategy could be easily adapted to nonviral T cell genome engineering using CRISPR–Cas9 and virus-free single-stranded DNA as a template donor, as recently demonstrated for IL-7–IL-15–expanded blood-derived T_{SCM} cells at a clinical scale (*31*).

One potential limitation of T cell–based therapy for FHL is the lack of repaired NK cells, which may be required for optimal disease protection (*63*). Memory T cells may be able to functionally substitute for NK cells, because they can acquire innate properties such as responsiveness to innate cytokines and a "primed" state for interferon gamma (IFN-γ) production (*64*). However, it is conceivable that this problem could be addressed in the future with optimized forms of gene therapy using autologous hematopoietic stem cells, either alone or in combination with repaired T cells. Such therapies may even supplant the current allo-HSCT treatment associated with high mortality rates (*9, 34, 65*). In this respect, we recently demonstrated that the *PRF1* locus can be repaired precisely and efficiently in human hematopoietic stem and progenitor cells using an approach that minimizes unwanted on- and off-target events (*48*).

For autologous T cells (as opposed to hematopoietic progenitor cells), unwanted on- and off-target events may be less critical, given that autologous gene-modified T cells have been used safely, without evidence of malignant transformation, for hundreds of patients in the context of cancer treatment (*53*). However, before precise gene editing can be applied in the clinic, careful assessment of potential off-target sites is required. GUIDE-seq analysis for our guide RNAs indicated high specificity, suggesting clinical suitability for *PRF1* guide RNA sg*PRF1.2* and an intergenic off-target site for *PRF1* guide RNA sg*PRF1.1*. Off-target activity of the second *PRF1* guide could be remedied by using an engineered high-fidelity Cas9 (*66*),

whereas our guide RNA for the *UNC13D* patient-specific mutation may not be suitable for clinical application.

Our study does not clarify whether repaired T cells expressing suboptimal levels of the repaired protein would be able to overcome clinical disease in patients (*67*). An additional challenge is the heterogeneity of the clinical presentation of patients with primary hereditary HLH. Forms of the disease caused by T cell–based genetic defects can present with different severities and ages of onset (*1, 4, 9*). Clinical trials will therefore be needed to establish whether engrafted repaired memory T cells are able to clear infectious challenges, and if so, for how long such protection may last in various patient subgroups (*34*). Overall, the present work establishes gene repair in autologous T cells as a promising therapeutic approach for human FHL in a preclinical model, and demonstrates its feasibility for T cells from patients.

MATERIALS AND METHODS

Study design

Research objectives

We sought to determine the feasibility of precisely repairing genes required for cytotoxic functions in potentially long-lived memory T cells, including mutated T cells isolated from FHL patients and to explore the therapeutic potential of such cells in a mouse model of FHL or their suitability for clinical translation in functional assays with repaired patient T cells.

Overall study design

We performed controlled laboratory experiments. We first used primary mouse T cells to establish an efficient CRISPR–Cas9–AAV gene repair protocol in the presence and absence of NHEJ small-molecule inhibitor M3814. We then tested whether repaired cells could prevent or cure lethal HLH disease in a mouse model of EBV-triggered HLH in the context of perforin-1 deficiency. We subsequently obtained and ex vivo–expanded mutant T cells from blood samples of an FHL2 (perforin-1 deficiency) and an FHL3 (Munc13-4 deficiency) patient. We gene-repaired mutant patient T cells and tested their cytotoxic effector function in cell culture experiments.

Research subjects

Genetically defined mouse strains, primary mouse T cells and human T cells isolated from healthy donors and patients.

Data collection

Given the discovery research nature of the study, no predefined power calculations for sample size were used and experiments were not randomized or blinded. No data points or outliers were excluded from the analysis. The number of independent biological replicates is given in each respective figure legend or table. Mouse sample size calculations were based on previous experiments in an earlier study by us (*25*). In order to prevent unnecessary suffering before death due to terminal illness, termination criteria and humane endpoints for survival analysis of mice were predefined based on the same earlier study (*25*) (Figs. 1 and 4). Upon induction of LMP-expression by tamoxifen, mice were closely monitored for development of end-stage disease by visual observation (strongly reduced activity, hunched posture, and ungroomed fur) and were sacrificed if they manifested all of these symptoms. Symptom-free animals showed none of these symptoms.

Mouse strains

Mouse strains *Cd19*-Cre^{ERT2}(*68*), R26LMP1^{flSTOP}(*69*), R26LMP2A^{flSTOP} (*25*) and *Prf1*$^{-/-}$ (*26*) have previously been described. Animal care adhered to the guidelines of the Institutional

Animal Care and Use Committee of the MDC. Animal experiments were reviewed and approved by the Landesamt für Gesundheit und Soziales Berlin (LAGeSo # G0213/16).

Cell lines

All cells and cell lines were incubated at 37°C, 5% CO_2. The mouse LMP1-expressing B lymphoma cell line 2726L (*25*) was cultured in B cell medium (DMEM (ThermoFisher Scientific, 11960044) supplemented with 10% FCS, 1X non-essential amino acids, 1X penicillin–streptomycin, 1X sodium pyruvate, 1X GlutaMAX™, and 52 µM β-mercaptoethanol). HEK293T cells used for AAV production were maintained in DMEM (ThermoFisher Scientific, 11960044) supplemented with 10% FCS, 1X sodium pyruvate, 1X GlutaMAX™, and 1X penicillin–streptomycin. BJAB cells were cultured in RPMI 1640 (ThermoFisher Scientific, 21875034) supplemented with 10% FCS, 1X GlutaMAX™, and 1X penicillin–streptomycin.

T cell isolation and culture

Mouse cells

Total T cells were isolated from spleens of C57BL/6 or *Prf1*$^{-/-}$ mice (*26*) (Pan T Cell Isolation Kit II, mouse, Miltenyi Biotec) and activated with plate-bound anti-CD3ε (10 µg/ml; 145-2C11, Biolegend, 100-301) and anti-CD28 (5 µg/ml; Clone 37.51, Biolegend, 102101) in the presence of mouse IL-2 (25 ng/ml; Peprotech, 212-12) for 2 days. Activated mouse T cells were further cultured in the presence of mouse IL-2 in B cell medium.

Human cells

CD8 T cells isolated from peripheral blood of healthy donors by positive selection of $CD8^+$ T cells ($CD8^+$ T cell Isolation kit, Miletnyi Biotec, 130-096-495) or unpurified bulk T cells within peripheral mononuclear cells (PBMCs) were activated with ImmunoCult™ Human CD3/CD28/CD2 T Cell Activator (STEMCELL Technologies, 10970) in the presence of human IL-7 (5 ng/ml, Peprotech, AF-200-07) and human IL-15 (5 ng/ml, Peprotech, AF-200-15) for 3 days. Activated human T cells were further cultured in ImmunoCult™ -XF T Cell Expansion Medium (STEMCELL Technologies, 10981) with human IL-2, or human IL-7 (5 ng/ml, Peprotech, AF-200-07) and human IL-15 (5 ng/ml, Peprotech, AF-200-15) for 7 days. At this point aliquots of expanded healthy donor-derived bulk T cells were frozen for later use. Healthy donor CD8 T cells were reactivated with ImmunoCult™ Human CD3/CD28/CD2 T Cell Activator (STEMCELL Technologies) with human IL-2 (25 ng/ml; Peprotech, 200-02) for 2 days, followed by flow cytometry analysis and used as staining controls for BV421-PD1 and PE/Dazzle594-TIGIT.

FHL patient–derived cells

In order to expand and sustain preferentially T_{SCM}-like cells, PBMCs were activated as described above for 3 days. Bulk T cells were then expanded for another 5-7 days in the presence of human IL-7 and human IL-15. At this point, multiple aliquots of expanded patient-derived bulk T cells were frozen for later use.

Flow cytometry analysis and FACS

Single-cell suspensions were prepared from spleens and livers of the experimental mice as described (*25*) and strained through a 35 µm nylon mesh, before staining with antibodies (table S6). Fc receptors were blocked by incubation with 5 µg/ml FcγR antibody (anti-mouse CD16/32) for 10 min at 4°C. Surface antigens were then stained with fluorescent-conjugated antibodies for 15 min at 4°C (see table S6). The cells were finally washed with MACS buffer (PBS/1%BSA) and analyzed on a BD Fortessa (BD Biosciences). Cell survival was defined as fraction of live cells (measured by DAPI staining or LIVE/DEAD™ Fixable Dead Cell Stain Kits (ThermoFisher Scientific, L34981 (Aqua) L34957 (Near-IR)). Cell sorting was performed on a BD FACSAria^{TM} III Cell Sorter (BD Biosciences). FlowJo software (v.10, FlowJo, BD) was used for cell analysis.

In vivo mouse experiments

In order to generate perforin-1–deficient LMP1-specific memory T cells, 0.4 mg tamoxifen (Sigma, T5648) dissolved in sunflower oil (Sigma, S5007) was administered once by oral gavage to *Cd19-Cre^{ERT2}*;R26LMP^{flSTOP};*Prf1$^{-/-}$* mice (Fig. 3A). At least 28 days after tamoxifen administration, CD8^{+}CD44^{hi} memory T cells isolated from the spleen by FACS were activated by coculture with γ-irradiated (9 Gy) mouse LMP1-expressing B lymphoma cell line 2726L (*25*) for 3 days. Memory T cells were then used for gene targeting (see below) and expanded for 4 days prior to adoptive transfer (Fig. 4A). One million repaired mCherry-positive T cells were transferred into *Cd19*-Cre^{ERT2};R26LMP^{flSOTP};*Prf1$^{-/-}$* mice either 1 day before, or 1 to 2 days after administration of 4 mg of tamoxifen. Mice were closely monitored visual observation for the development of disease (strongly reduced activity, hunched posture, and ungroomed fur) and were sacrificed if they manifested all of these symptoms (humane endpoint to prevent unnecessary suffering before death). Symptom-free mice appeared normal and did not show any sign of disease.

AAV donor template cloning and recombinant AAV production

All recombinant AAV vectors generated in this study are based on pAAV-GFP (Cell Biolabs, AAV-400), which contains inverted terminal repeats (ITRs). Plasmids were created with the NEBuilder HiFi DNA Assembly Cloning kit (New England Biolabs, E5520S). To generate plasmid vectors pAAV-B2m-mCherry-pA (Fig. S1), pAAV-B2M-T2A-mCherry-pA (fig. S2), pAAV-*Prf1*-ires-mCherry (Fig. 2B), pAAV-*Prf1*-mock-ires-mCherry (Fig. 2B), pAAV-*PRF1*-Exon3 (Fig. 5B and table S3), pAAV-*PRF1*-T2A-cDNA (Fig. 5B and table S4), and pAAV-*UNC13D*-Exon10 (Fig. 7A), the respective left and right homology arms were amplified from genomic DNA of C57BL/6 or *Prf1$^{-/-}$* mice or PBMCs of healthy donors. Based on previous evidence (*70*), we aimed for a minimum length of 500 bp and up to 1 kb or more if the packaging capacity of AAV allowed for this. The nucleotide sequences of the *PRF1* exon 3, the *PRF1* cDNA and the *UNC13D* exon 10 were optimized for expression in mammalian cells on the transcriptional, mRNA stability and translational level and de novo custom synthesized (GeneOptimizer Software, GeneArt Gene Synthesis Services, ThermoFisher) (tables S3 to S5). AAV production was described previously (*29, 39*). AAV-DJ and AAV6 were used for mouse and human T cells, respectively.

Genome editing of mouse and human T cells

sgRNAs were designed by CrispRGold 1.1 (*71*) and purchased from IDT (table S7). To generate sgRNA complexes, crRNA and tracrRNA were combined at a 1:1 molar ratio, annealed at 95°C for 5 min, and ramped down to room temperature. Cas9 protein (Alt-R S. p. Cas9 Nuclease V3) was either purchased (Integrated DNA Technologies, 1081059) or produced in-house. Ribonucleoprotein particles (RNPs) were complexed at a Cas9–sgRNA molar ratio of 1:2 at 25°C for 10 min before electroporation. Based on the amount of Cas9 protein, 50 pmol of RNPs was used per 5×10^5 cells. A total of 3-5×10^5 cells were suspended in 20 µl of P3 electroporation buffer (Lonza, V4XP-3032) containing corresponding amounts of RNPs and electroporated using a Lonza 4D Nucleofector (Program DN-100 for mouse and EH-100 for human cells). Cells were plated at 2.5×10^5 cells per mililiter following electroporation in the cytokine-supplemented media described above with or without M3814 (5 µM; MedChemExpress, 1637542-33-6) (*27, 31*). Immediately following electroporation, AAV-DJ and AAV6 were added to mouse T cells (1-2×10^7 vector genomes per cell) and human T cells (1-2×10^6 vector genomes per cell), respectively. The medium was changed the following day. For gene targeting, healthy donor PBMC-derived T cells or patient-derived T cells, expanded and frozen down as described above, were thawed and reactivated with ImmunoCult™ Human CD3/CD28/CD2 T Cell Activator for 2 days in the presence of human IL-2 (25 ng/ml). After gene targeting, healthy donor-derived T cells or patient-derived T cells were expanded for 4 days with human IL-2 and further expanded for an additional 1-2 days with human IL-7 (5 ng/ml) and human IL-15 (5 ng/ml). They were then subjected to flow cytometry analysis, genomic DNA extraction, restimulation for subsequent analyses (killing or degranulation assays and intracellular perforin staining), or frozen and stored in liquid nitrogen for later use. When high numbers of cells were needed, patient-derived T cells were restimulated and expanded.

Analysis of gene-targeting efficiency

Flow cytometry

Between 4 to 8 days post targeting, T cells were harvested, stained with DAPI or the LIVE/DEAD™ Fixable Aqua Dead Cell Stain Kit and the percentage of edited, mCherry-positive cells was determined after gating for viable (DAPI-negative or Aqua-negative) cells.

PCR to confirm correct integration site, cloning, and Sanger sequencing

Genomic DNA from the targeted T cells was extracted using the QuickExtract DNA extraction kit (Lucigen, QE09050). To confirm the correct integration site, the targeted site was amplified using the PrimeSTAR GXL DNA polymerase (TAKARA, R050B) with gene-specific primers (table S8). Purified PCR products were cloned into sequencing vector pJET1.2/Blunt (CloneJET PCR cloning kit, Thermo Scientific, K1231) (Fig. 6, Fig. 7, Fig. S1, and Fig. S2). Colonies were picked into 96-well LB agar plates and plasmids were sequenced (LGC, Biosearch Technologies), and non-targeted, HDR, and NHEJ events counted. In case of Fig. 2E, gel electrophoresis yielded two bands, a smaller band (~ 2.25 kb) corresponding in size to a deletion of the entire sequence between the two single guide RNAs used (large deletion) and a larger

band (~4.5 kb) corresponding to HDR events, NHEJ events (small indels), or non-targeted sequences. We used Image J (NIH, Bethesda, MD) to quantify the relative amounts of DNA in each band. In order to determine the number of non-targeted, HDR and NHEJ events on the targeted locus, the larger band (~4.5 kb) was extracted for nested PCR, cloning and sequencing as above.

Ex vivo mouse T cell proliferation assay

$CD8^+CD44^{hi}$ T cells were isolated by FACS from *Cd19*-Cre^{ERT2};$R26LMP^{flSOTP}$; $Prf1^{-/-}$ mice at least 28 days after tamoxifen administration (0.4 mg). Cells were then labeled with 5 μM CellTrace Violet (Invitrogen, C34571) at 37°C for 15 min. The labeled cells were washed with B cell medium and cocultured for 3 days with γ-irradiated (9 Gy) LMP1-expressing B lymphoma cells, followed by flow cytometry analysis.

Intracellular perforin-1 staining

Mouse T cells

$mCherry^+$ sorted perforin-1–repaired or mock-repaired CD8 T cells were either activated with PMA/ionomycin for 4 hours (Sigma, P8139 and Sigma, I0634) in the presence of 1X brefeldin A solution (BioLegend, 420601) or activated with LMP1-expressing B lymphoma cell line (2726L)(*25*) overnight, followed by DAPI staining (1 μg/ml) for exclusion of dead cells before fixation and processing for intracellular of perforin (APC anti-mouse Perforin, BioLegend, 154304) according to the BD Cytofix/Cytoperm kit instructions (BD Biosciences, 554714).

Human T cells

Targeted patient-derived T cells were reactivated with ImmunoCult™ Human CD3/CD28/CD2 T Cell Activator (STEMCELL Technologies) and human IL-2 for 2 days and incubated with BJAB cells at a 1:1 ratio with 5 ng/ml of blinatumomab (Blincyto; Amgen Europe B. V.), a CD19–CD3 bispecific T cell engager (BiTE) antibody, which enables human T cells to recognize malignant $CD19^+$ B cells (*43*). Reactivated T cells from patients or targeted T cells from healthy donors were stimulated with PMA (50 ng/ml) and ionomycin (500 ng/ml) for 6 hours in the presence of 1X Brefeldin A solution. T cells were stained with the LIVE/DEAD™ Fixable Near-IR Dead Cell Stain Kit (ThermoFisher Scientific, L34981) for dead-cell exclusion before fixation and processing for intracellular staining of precursor and mature forms of perforin-1 (PE anti-human perforin-1, clone B-D48, BioLegend, 353304) (*72*) and staining of CD8 T cells by BV785-CD8 (SK1, BioLegend, 344740) according to the BD Cytofix/Cytoperm kit instructions.

Degranulation assay by detection of CD107a release (human T cells)

To measure degranulation in response to target cell stimulation, gene-repaired or non-targeted T cells (effector cells), reactivated with ImmunoCult™ Human CD3/CD28/CD2 T Cell Activator for 2 days in the presence of human IL-2 were cocultured with target cells (BJAB cells) at a 1:1 ratio in the presence of 5 ng/ml of blinatumomab, a CD19–CD3 BiTE antibody (*43*). One microliter of PE-CD107a (H4A3, Biolegend, 328608) antibody was added to stimulated T cells

to detect expression of CD107a. Four hours after coculture, cells were collected and stained with BV785-CD8 for 15 min at 4°C. The cells were then washed with MACS buffer (PBS/1%BSA) and analyzed on a BD Fortessa. Cell survival was defined as fraction of live cells measured by DAPI staining.

IncuCyte live-cell analysis of cytotoxic T cell killing (human T cells)

Ninety-six-well plates were coated with 50 µl of 5 µg/ml of retronectin (Takara, T100B) per well, incubated for 60 min. Then retronectin was removed, followed by another 60 min incubation at room temperature. Gene-repaired or non-targeted T cells (effector cells), preactivated with ImmunoCult™ Human CD3/CD28/CD2 T Cell Activator for 2 days with human IL-2, and BJAB target cells (expressing mCherry reporter) were centrifuged at 300 g for 5 minutes and resuspended in ImmunoCult™ -XF T Cell Expansion Medium with human IL-2. Twenty thousand BJAB cells in 100 µl per well were incubated for 30 min at room temperature and 1 hour at 37°C. Forty thousand gene-repaired or non-targeted T cells in 100 µl per well together with 5 ng/ml blinatumomab CD19–CD3 BiTE antibody (*43*) were carefully added and cells were allowed to settle at room temperature for 30 min before transfer to an IncuCyte Live Cell Imaging System (IncuCyte® S3 Live-Cell Analysis Instrument, SARTORIUS) inside a cell incubator (37°C, 5% CO_2). Images were taken every hour for 24 hours using the IncuCyte software. The total red object integrated intensity (RCU×µm^2 per image) from live mCherry-expressing target cells was calculated per each time point. A killing index was calculated by normalizing the total red object integrated intensity (RCU×µm^2 per image) of each time point to 0 hours.

Genome-wide identification of off-target sites with GUIDE-seq

For Tn5-modified GUIDE-seq experiments (*48*) patient-derived T cells were reactivated with ImmunoCult™ Human CD3/CD28/CD2 T Cell Activator (STEMCELL Technologies) and human IL-2 (25 ng/ml) for 2 days, and a total of 3×10^5 human T cells were electroporated with RNPs and 50 pmol of duplexed end-protected dsODN (Lonza 4D Nucleofector, Program EO-115) with or without M3814 (5 µM; MedChemExpress, 1637542-33-6). The medium was changed the next day. The targeted cells were harvested 4 days after electroporation. Dead cells were removed (EasySep™ Dead Cell Removal (Annexin V) Kit; STEMCELL Technologies, 17899) and genomic DNA was extracted from 2-5×10^5 targeted T cells (GenFind V3 Reagent Kit; Beckman Coulter, C34880). Genomic DNA (100 ng) was fragmented using *Tn5* transposase (IIlumina, 20034197) in 20 µl of reaction at 55°C for 7 min. Tagmented DNA fragments were purified by using Zymo DNA Clean and Concentrator-5 according to the manufacturer's protocol (Zymo Research, D4014). GUIDE-seq libraries were prepared as previously described (*49, 50*) with specific primer sets (table S8) and loaded onto Illumina MiniSeq or MiSeq for deep sequencing. Samples were sequenced to a minimum read depth of 2.5 million (*PRF1*) and 1 million (*UNC13D*).

Processing of the GUIDE-seq reads and off-target cleavage profiling

The R pipeline for processing and visualization of GUIDE-seq reads according to (*49, 73*) is available (*74*). Paired-end base-called Illumina reads were assembled using PEAR software (*75*)

and filtered based on the presence of full-length dsODN sequence at the start of the read (one mismatch allowed). dsODN sequence was cropped using R script and the resulting reads were aligned to the GRCh38.p14 human genome assembly using minimap2 (*76*). Unspecific amplification products and reads aligning to dsODN integration sites were discriminated using the following criterion: at least two reads mapped to the opposite strands with the shared start/end coordinate, with 5 nt indel allowed. The off-target sites were annotated with UCSC Genome Browser human gene database and aligned to the sgRNA sequences using R script and visualized using ggplot2 library (*77, 78*). Off-target cleavage sites with more than seven mismatches to the intended target sequence (*49, 73*) were removed manually from the visualization output (fig. S6B).

Statistical analyses

Eight-to-twelve-week old male and female mice were used in similar numbers for comparisons between groups. Mouse sample-size calculations were based on results of previous experiments (mouse model for EBV-triggered FHL2) (*25*). To calculate statistical significance of symptom-free survival, we used Kaplan-Meier survival analysis with the log-rank (Mantel–Cox) test (conservative) in GraphPad Prism 9. Medians and statistical significance were calculated in GraphPad Prism 9 by a non-parametric test (two-tailed Mann–Whitney *U* -test with exact *P* values). All tests were performed using 95% confidence levels, and $P > 0.05$ was considered not significant (ns).

Supplementary Materials

Supplementary Text

Figs. S1 to S6

Tables S1 to S8

Data files S1 and S2

References and Notes

1. H. Al-Samkari, N. Berliner, Hemophagocytic Lymphohistiocytosis. *Annu Rev Pathology Mech Dis* **13**, 1–23 (2017).

2. N. R. Maakaroun, A. Moanna, J. T. Jacob, H. Albrecht, Viral infections associated with haemophagocytic syndrome. *Rev Med Virol* **20**, 93–105 (2010).

3. C. E. Terrell, M. B. Jordan, Perforin deficiency impairs a critical immunoregulatory loop involving murine CD8+ T cells and dendritic cells. *Blood* **121**, 5184–5191 (2013).

4. S. W. Canna, R. A. Marsh, Pediatric hemophagocytic lymphohistiocytosis. *Blood* **135**, 1332–1343 (2020).

5. G. E. Janka, K. Lehmberg, Hemophagocytic lymphohistiocytosis: pathogenesis and treatment. *Hematology* **2013**, 605–611 (2013).

6. G. Ménasché, J. Feldmann, A. Fischer, G. D. S. Basile, Primary hemophagocytic syndromes point to a direct link between lymphocyte cytotoxicity and homeostasis. *Immunol Rev* **203**, 165–179 (2005).

7. V. Chaturvedi, R. A. Marsh, A. Z. Lorenz, E. Owsley, V. Chaturvedi, T. Nguyen, J. Goldman, M. M. Henry, J. Greenberg, S. Ladisch, M. L. Hermiston, M. R. Jeng, A. Naqvi, C. E. Allen, H. R. Wong, M. B. Jordan, T cell activation profiles distinguish hemophagocytic lymphohistiocytosis and early sepsis. *Blood* **137**, 2337–2346 (2020).

8. S. Ammann, K. Lehmberg, U. Z. Stadt, G. Janka, A. Rensing-Ehl, C. Klemann, M. Heeg, S. Bode, I. Fuchs, S. Ehl, H. study of the GPOH, Primary and secondary hemophagocytic lymphohistiocytosis have different patterns of T-cell activation, differentiation and repertoire. *Eur J Immunol* **47**, 364–373 (2017).

9. C. Gholam, S. Grigoriadou, K. C. Gilmour, H. B. Gaspar, Familial haemophagocytic lymphohistiocytosis: advances in the genetic basis, diagnosis and management. *Clin Exp Immunol* **163**, 271–283 (2011).

10. M. B. Jordan, C. E. Allen, S. Weitzman, A. H. Filipovich, K. L. McClain, How I treat hemophagocytic lymphohistiocytosis. *Blood* **118**, 4041–4052 (2011).

11. E. Bergsten, A. Horne, M. Aricó, I. Astigarraga, R. M. Egeler, A. H. Filipovich, E. Ishii, G. Janka, S. Ladisch, K. Lehmberg, K. L. McClain, M. Minkov, S. Montgomery, V. Nanduri, D. Rosso, J.-I. Henter, Confirmed efficacy of etoposide and dexamethasone in HLH treatment: long-term results of the cooperative HLH-2004 study. *Blood* **130**, 2728–2738 (2017).

12. J. Henter, A. Horne, M. Aricó, R. M. Egeler, A. H. Filipovich, S. Imashuku, S. Ladisch, K. McClain, D. Webb, J. Winiarski, G. Janka, HLH-2004: Diagnostic and therapeutic guidelines for hemophagocytic lymphohistiocytosis. *Pediatr Blood Cancer* **48**, 124–131 (2007).

13. H. Trottestam, E. Berglöf, A. Horne, E. Onelöv, K. Beutel, K. Lehmberg, E. Sieni, T. Silfverberg, M. Aricò, G. Janka, J. Henter, Risk factors for early death in children with haemophagocytic lymphohistiocytosis. *Acta Paediatr* **101**, 313–318 (2012).

14. K. Lehmberg, M. H. Albert, R. Beier, K. Beutel, B. Gruhn, N. Kröger, R. Meisel, A. Schulz, D. Stachel, W. Woessmann, G. Janka, I. Müller, Treosulfan-based conditioning regimen for children and adolescents with hemophagocytic lymphohistiocytosis. *Haematologica* **99**, 180–184 (2014).

15. R. A. Marsh, K. Hebert, S. Kim, C. C. Dvorak, V. M. Aquino, K. S. Baker, D. Chellapandian, B. D. Saldaña, C. N. Duncan, M. J. Eckrich, G. E. Georges, T. S. Olson, M. A. Pulsipher, S. Shenoy, E. Stenger, M. V. Lugt, L. C. Yu, A. R. Gennery, M. Eapen, Comparison

of hematopoietic cell transplant conditioning regimens for hemophagocytic lymphohistiocytosis disorders. *J Allergy Clin Immun* **149**, 1097-1104.e2 (2022).

16. H. Trottestam, A. Horne, M. Aricò, R. M. Egeler, A. H. Filipovich, H. Gadner, S. Imashuku, S. Ladisch, D. Webb, G. Janka, J.-I. Henter, for the H. Society, Chemoimmunotherapy for hemophagocytic lymphohistiocytosis: long-term results of the HLH-94 treatment protocol. *Blood* **118**, 4577–4584 (2011).

17. L. Biasco, S. Scala, L. B. Ricci, F. Dionisio, C. Baricordi, A. Calabria, S. Giannelli, N. Cieri, F. Barzaghi, R. Pajno, H. Al-Mousa, A. Scarselli, C. Cancrini, C. Bordignon, M. G. Roncarolo, E. Montini, C. Bonini, A. Aiuti, In vivo tracking of T cells in humans unveils decade-long survival and activity of genetically modified T memory stem cells. *Sci Transl Med* **7**, 273ra13-273ra13 (2015).

18. G. Oliveira, E. Ruggiero, M. T. L. Stanghellini, N. Cieri, M. D'Agostino, M. D'Agostino, R. Fronza, C. Lulay, F. Dionisio, S. Mastaglio, R. Greco, J. Peccatori, A. Aiuti, A. Ambrosi, L. Biasco, A. Bondanza, A. Lambiase, C. Traversari, L. Vago, C. von Kalle, M. Schmidt, C. Bordignon, F. Ciceri, C. Bonini, Tracking genetically engineered lymphocytes long-term reveals the dynamics of T cell immunological memory. *Sci Transl Med* **7**, 317ra198-317ra198 (2015).

19. L. Gattinoni, D. E. Speiser, M. Lichterfeld, C. Bonini, T memory stem cells in health and disease. *Nat Med* **23**, 18–27 (2017).

20. N. Cieri, G. Oliveira, R. Greco, M. Forcato, C. Taccioli, B. Cianciotti, V. Valtolina, M. Noviello, L. Vago, A. Bondanza, F. Lunghi, S. Marktel, L. Bellio, C. Bordignon, S. Bicciato, J. Peccatori, F. Ciceri, C. Bonini, Generation of human memory stem T cells after haploidentical T-replete hematopoietic stem cell transplantation. *Blood* **125**, 2865–2874 (2015).

21. E. Sieni, V. Cetica, Y. Hackmann, M. L. Coniglio, M. D. Ros, B. Ciambotti, D. Pende, G. Griffiths, M. Aricò, Familial Hemophagocytic Lymphohistiocytosis: When Rare Diseases Shed Light on Immune System Functioning. *Front Immunol* **5**, 167 (2014).

22. J. Feldmann, I. Callebaut, G. Raposo, S. Certain, D. Bacq, C. Dumont, N. Lambert, M. Ouachée-Chardin, G. Chedeville, H. Tamary, V. Minard-Colin, E. Vilmer, S. Blanche, F. L. Deist, A. Fischer, G. de S. Basile, Munc13-4 Is Essential for Cytolytic Granules Fusion and Is Mutated in a Form of Familial Hemophagocytic Lymphohistiocytosis (FHL3). *Cell* **115**, 461–473 (2003).

23. M. Heeg, S. Ammann, C. Klemann, M. Panning, V. Falcone, H. Hengel, K. Lehmberg, U. zur Stadt, K. Wustrau, G. Janka, S. Ehl, Is an infectious trigger always required for primary hemophagocytic lymphohistiocytosis? Lessons from in utero and neonatal disease. *Pediatr Blood Cancer* **65**, e27344 (2018).

24. G. S. Taylor, H. M. Long, J. M. Brooks, A. B. Rickinson, A. D. Hislop, The Immunology of Epstein-Barr Virus–Induced Disease. *Annu Rev Immunol* **33**, 1–35 (2015).

25. T. Wirtz, T. Weber, S. Kracker, T. Sommermann, K. Rajewsky, T. Yasuda, Mouse model for acute Epstein–Barr virus infection. *Proc National Acad Sci* **113**, 13821–13826 (2016).

26. D. Kägi, B. Ledermann, K. Bürki, P. Seiler, B. Odermatt, K. J. Olsen, E. R. Podack, R. M. Zinkernagel, H. Hengartner, Cytotoxicity mediated by T cells and natural killer cells is greatly impaired in perforin-deficient mice. *Nature* **369**, 31–37 (1994).

27. S. Riesenberg, M. Chintalapati, D. Macak, P. Kanis, T. Maricic, S. Pääbo, Simultaneous precise editing of multiple genes in human cells. *Nucleic Acids Res* **47**, e116–e116 (2019).

28. A. Seki, S. Rutz, Optimized RNP transfection for highly efficient CRISPR/Cas9-mediated gene knockout in primary T cells. *J. Exp. Med.* **215**, 985–997 (2018).

29. N. T. Tran, T. Sommermann, R. Graf, J. Trombke, J. Pempe, K. Petsch, R. Kühn, K. Rajewsky, V. T. Chu, Efficient CRISPR/Cas9-Mediated Gene Knockin in Mouse Hematopoietic Stem and Progenitor Cells. *Cell Reports* **28**, 3510-3522.e5 (2019).

30. D. Grimm, J. S. Lee, L. Wang, T. Desai, B. Akache, T. A. Storm, M. A. Kay, In Vitro and In Vivo Gene Therapy Vector Evolution via Multispecies Interbreeding and Retargeting of Adeno-Associated Viruses. *J. Virol.* **82**, 5887–5911 (2008).

31. B. R. Shy, V. S. Vykunta, A. Ha, A. Talbot, T. L. Roth, D. N. Nguyen, W. G. Pfeifer, Y. Y. Chen, F. Blaeschke, E. Shifrut, S. Vedova, M. R. Mamedov, J.-Y. J. Chung, H. Li, R. Yu, D. Wu, J. Wolf, T. G. Martin, C. E. Castro, L. Ye, J. H. Esensten, J. Eyquem, A. Marson, High-yield genome engineering in primary cells using a hybrid ssDNA repair template and small-molecule cocktails. *Nat Biotechnol* , 1–11 (2022).

32. M. T. J. van Bussel, A. Awada, M. J. A. de Jonge, M. Mau-Sørensen, D. Nielsen, P. Schöffski, H. M. W. Verheul, B. Sarholz, K. Berghoff, S. E. Bawab, M. Kuipers, L. Damstrup, I. Diaz-Padilla, J. H. M. Schellens, A first-in-man phase 1 study of the DNA-dependent protein kinase inhibitor peposertib (formerly M3814) in patients with advanced solid tumours. *Brit J Cancer* **124**, 728–735 (2021).

33. W. A. Nyberg, J. Ark, A. To, S. Clouden, G. Reeder, J. J. Muldoon, J.-Y. Chung, W. H. Xie, V. Allain, Z. Steinhart, C. Chang, A. Talbot, S. Kim, A. Rosales, L. P. Havlik, H. Pimentel, A. Asokan, J. Eyquem, An evolved AAV variant enables efficient genetic engineering of murine T cells. *Cell* **186**, 446-460.e19 (2023).

34. S. Ghosh, M. Carmo, M. Calero-Garcia, I. Ricciardelli, J. C. B. Ogando, M. P. Blundell, A. Schambach, P. G. Ashton-Rickardt, C. Booth, S. Ehl, K. Lehmberg, A. J. Thrasher, H. B. Gaspar, T-cell gene therapy for perforin deficiency corrects cytotoxicity defects and prevents hemophagocytic lymphohistiocytosis manifestations. *J Allergy Clin Immunol* **142**, 904-913.e3 (2018).

35. U. Palendira, C. Low, A. I. Bell, C. S. Ma, R. J. M. Abbott, T. G. Phan, D. S. Riminton, S. Choo, J. M. Smart, V. Lougaris, S. Giliani, R. H. Buckley, B. Grimbacher, F. Alvaro, A. D.

Klion, K. E. Nichols, S. Adelstein, A. B. Rickinson, S. G. Tangye, Expansion of somatically reverted memory CD8+ T cells in patients with X-linked lymphoproliferative disease caused by selective pressure from Epstein-Barr virus. *J Exp Medicine* **209**, 913–924 (2012).

36. P. Graef, V. R. Buchholz, C. Stemberger, M. Flossdorf, L. Henkel, M. Schiemann, I. Drexler, T. Höfer, S. R. Riddell, D. H. Busch, Serial Transfer of Single-Cell-Derived Immunocompetence Reveals Stemness of CD8+ Central Memory T Cells. *Immunity* **41**, 116–126 (2014).

37. N. Cieri, B. Camisa, F. Cocchiarella, M. Forcato, G. Oliveira, E. Provasi, A. Bondanza, C. Bordignon, J. Peccatori, F. Ciceri, M. T. Lupo-Stanghellini, F. Mavilio, A. Mondino, S. Bicciato, A. Recchia, C. Bonini, IL-7 and IL-15 instruct the generation of human memory stem T cells from naive precursors. *Blood* **121**, 573–584 (2013).

38. M. Schmueck-Henneresse, R. Sharaf, K. Vogt, B. J. D. Weist, S. Landwehr-Kenzel, H. Fuehrer, A. Jurisch, N. Babel, C. M. Rooney, P. Reinke, H.-D. Volk, Peripheral Blood–Derived Virus-Specific Memory Stem T Cells Mature to Functional Effector Memory Subsets with Self-Renewal Potency. *J Immunol* **194**, 5559–5567 (2015).

39. N. T. Tran, R. Graf, A. Wulf-Goldenberg, M. Stecklum, G. Strauß, R. Kühn, C. Kocks, K. Rajewsky, V. T. Chu, CRISPR-Cas9-Mediated ELANE Mutation Correction in Hematopoietic Stem and Progenitor Cells to Treat Severe Congenital Neutropenia. *Mol Ther* **28**, 2621–2634 (2020).

40. M. Pavel-Dinu, V. Wiebking, B. T. Dejene, W. Srifa, S. Mantri, C. E. Nicolas, C. Lee, G. Bao, E. J. Kildebeck, N. Punjya, C. Sindhu, M. A. Inlay, N. Saxena, S. S. DeRavin, H. Malech, M. G. Roncarolo, K. I. Weinberg, M. H. Porteus, Gene correction for SCID-X1 in long-term hematopoietic stem cells. *Nat Commun* **10**, 1634 (2019).

41. K. G. Ericson, B. Fadeel, S. Nilsson-Ardnor, C. Söderhäll, A. Samuelsson, G. Janka, M. Schneider, A. Gürgey, N. Yalman, T. Révész, R. M. Egeler, K. Jahnukainen, I. Storm-Mathiesen, Á. Haraldsson, J. Poole, G. de S. Basile, M. Nordenskjöld, J.-I. Henter, Spectrum of Perforin Gene Mutations in Familial Hemophagocytic Lymphohistiocytosis. *Am J Hum Genetics* **68**, 590–597 (2001).

42. A. Trizzino, U. zur Stadt, I. Ueda, K. Risma, G. Janka, E. Ishii, K. Beutel, J. Sumegi, S. Cannella, D. Pende, A. Mian, J.-I. Henter, G. Griffiths, A. Santoro, A. Filipovich, M. Aricò, H. S. H. S. group, Genotype–phenotype study of familial haemophagocytic lymphohistiocytosis due to perforin mutations. *J Med Genet* **45**, 15 (2008).

43. A. Löffler, P. Kufer, R. Lutterbüse, F. Zettl, P. T. Daniel, J. M. Schwenkenbecher, G. Riethmüller, B. Dörken, R. C. Bargou, A recombinant bispecific single-chain antibody, CD19 x CD3, induces rapid and high lymphoma-directed cytotoxicity by unstimulated T lymphocytes. *Blood* **95**, 2098–103 (2000).

44. E. Ishii, I. Ueda, R. Shirakawa, K. Yamamoto, H. Horiuchi, S. Ohga, K. Furuno, A. Morimoto, M. Imayoshi, Y. Ogata, M. Zaitsu, M. Sako, K. Koike, A. Sakata, H. Takada, T.

Hara, S. Imashuku, T. Sasazuki, M. Yasukawa, Genetic subtypes of familial hemophagocytic lymphohistiocytosis: correlations with clinical features and cytotoxic T lymphocyte/natural killer cell functions. *Blood* **105**, 3442–3448 (2005).

45. G. Galletti, G. D. Simone, E. M. C. Mazza, S. Puccio, C. Mezzanotte, T. M. Bi, A. N. Davydov, M. Metsger, E. Scamardella, G. Alvisi, F. D. Paoli, V. Zanon, A. Scarpa, B. Camisa, F. S. Colombo, A. Anselmo, C. Peano, S. Polletti, D. Mavilio, L. Gattinoni, S. K. Boi, B. A. Youngblood, R. E. Jones, D. M. Baird, E. Gostick, S. Llewellyn-Lacey, K. Ladell, D. A. Price, D. M. Chudakov, E. W. Newell, M. Casucci, E. Lugli, Two subsets of stem-like CD8+ memory T cell progenitors with distinct fate commitments in humans. *Nat Immunol* **21**, 1552–1562 (2020).

46. A. Hyrenius-Wittsten, Y. Su, M. Park, J. M. Garcia, J. Alavi, N. Perry, G. Montgomery, B. Liu, K. T. Roybal, SynNotch CAR circuits enhance solid tumor recognition and promote persistent antitumor activity in mouse models. *Sci Transl Med* **13** (2021), doi:10.1126/scitranslmed.abd8836.

47. L. M. McLane, M. S. Abdel-Hakeem, E. J. Wherry, CD8 T Cell Exhaustion During Chronic Viral Infection and Cancer. *Annu. Rev. Immunol.* **37**, 1–39 (2015).

48. N. T. Tran, E. Danner, X. Li, R. Graf, M. Lebedin, K. de la Rosa, R. Kühn, K. Rajewsky, V. T. Chu, Precise CRISPR-Cas–mediated gene repair with minimal off-target and unintended on-target mutations in human hematopoietic stem cells. *Sci. Adv.* **8**, eabm9106 (2022).

49. S. Q. Tsai, Z. Zheng, N. T. Nguyen, M. Liebers, V. V. Topkar, V. Thapar, N. Wyvekens, C. Khayter, A. J. Iafrate, L. P. Le, M. J. Aryee, J. K. Joung, GUIDE-seq enables genome-wide profiling of off-target cleavage by CRISPR-Cas nucleases. *Nat Biotechnol* **33**, 187–197 (2015).

50. N. L. Malinin, G. Lee, C. R. Lazzarotto, Y. Li, Z. Zheng, N. T. Nguyen, M. Liebers, V. V. Topkar, A. J. Iafrate, L. P. Le, M. J. Aryee, J. K. Joung, S. Q. Tsai, Defining genome-wide CRISPR–Cas genome-editing nuclease activity with GUIDE-seq. *Nat Protoc* **16**, 5592–5615 (2021).

51. K. Weißert, S. Ammann, T. Kögl, V. Dettmer-Monaco, C. Schell, T. Cathomen, S. Ehl, P. Aichele, Adoptive T cell therapy cures mice from active hemophagocytic lymphohistiocytosis (HLH). *Embo Mol Med* **14**, e16085 (2022).

52. F. Uddin, C. M. Rudin, T. Sen, CRISPR Gene Therapy: Applications, Limitations, and Implications for the Future. *Frontiers Oncol* **10**, 1387 (2020).

53. D. L. Wagner, U. Koehl, M. Chmielewski, C. Scheid, R. Stripecke, Review: Sustainable Clinical Development of CAR-T Cells – Switching From Viral Transduction Towards CRISPR-Cas Gene Editing. *Front Immunol* **13**, 865424 (2022).

54. M. Porteus, Genome Editing: A New Approach to Human Therapeutics. *Annu. Rev. Pharmacol. Toxicol.* **56**, 1–28 (2014).

55. W. A. Comrie, M. J. Lenardo, Molecular Classification of Primary Immunodeficiencies of T Lymphocytes. *Adv Immunol* **138**, 99–193 (2018).

56. C. E. Terrell, M. B. Jordan, Mixed hematopoietic or T-cell chimerism above a minimal threshold restores perforin-dependent immune regulation in perforin-deficient mice. *Blood* **122**, 2618–2621 (2013).

57. B. Hartz, R. Marsh, K. Rao, J.-I. Henter, M. Jordan, L. Filipovich, P. Bader, R. Beier, B. Burkhardt, R. Meisel, A. Schulz, B. Winkler, M. H. Albert, J. Greil, G. Karasu, W. Woessmann, S. Corbacioglu, B. Gruhn, W. Holter, J.-S. Kühl, P. Lang, M. G. Seidel, P. Veys, A. Löfstedt, S. Ammann, S. Ehl, G. Janka, I. Müller, K. Lehmberg, The minimum required level of donor chimerism in hereditary hemophagocytic lymphohistiocytosis. *Blood* **127**, 3281–3290 (2016).

58. T. Soheili, J. Rivière, I. Ricciardelli, A. Durand, E. Verhoeyen, A.-C. Derrien, C. Lagresle-Peyrou, G. de S. Basile, F.-L. Cosset, P. Amrolia, I. André-Schmutz, M. Cavazzana, Gene-corrected human Munc13-4–deficient CD8+ T cells can efficiently restrict EBV-driven lymphoproliferation in immunodeficient mice. *Blood* **128**, 2859–2862 (2016).

59. S. E. Takushi, N. Y. Paik, A. Fedanov, C. Prince, C. B. Doering, H. T. Spencer, S. Chandrakasan, Lentiviral Gene Therapy for Familial Hemophagocytic Lymphohistiocytosis Type 3, Caused by UNC13D Genetic Defects. *Hum Gene Ther* **31**, 626–638 (2020).

60. V. Dettmer, K. Bloom, M. Gross, K. Weissert, P. Aichele, S. Ehl, T. Cathomen, Retroviral UNC13D Gene Transfer Restores Cytotoxic Activity of T Cells Derived from Familial Hemophagocytic Lymphohistiocytosis Type 3 Patients In Vitro. *Hum Gene Ther* **30**, 975–984 (2019).

61. J. Gauthier, E. D. Bezerra, A. V. Hirayama, S. Fiorenza, A. Sheih, C. K. Chou, E. L. Kimble, B. S. Pender, R. M. Hawkins, A. Vakil, T.-D. Phi, R. N. Steinmetz, A. W. Jamieson, M. Bar, R. D. Cassaday, A. G. Chapuis, A. J. Cowan, D. J. Green, H.-P. Kiem, F. Milano, M. Shadman, B. G. Till, S. R. Riddell, D. G. Maloney, C. J. Turtle, Factors associated with outcomes after a second CD19-targeted CAR T-cell infusion for refractory B-cell malignancies. *Blood* **137**, 323–335 (2021).

62. A. Houghtelin, C. M. Bollard, Virus-Specific T Cells for the Immunocompromised Patient. *Front Immunol* **8**, 1272 (2017).

63. E. M. Mace, J. S. Orange, Emerging insights into human health and NK cell biology from the study of NK cell deficiencies. *Immunol Rev* **287**, 202–225 (2019).

64. C. A. Biron, M. Altfeld, Is There Natural Killer Cell Memory and Can It Be Harnessed by Vaccination?: Can Natural Killer and CD8 T Cells Switch Jobs? *Csh Perspect Biol* **10**, a029892 (2017).

65. M. Carmo, K. A. Risma, P. Arumugam, S. Tiwari, A. E. Hontz, C. A. Montiel-Equihua, M. E. Alonso-Ferrero, M. P. Blundell, A. Schambach, C. Baum, P. Malik, A. J. Thrasher, M. B.

Jordan, H. B. Gaspar, Perforin Gene Transfer Into Hematopoietic Stem Cells Improves Immune Dysregulation in Murine Models of Perforin Deficiency. *Mol Ther* **23**, 737–745 (2015).

66. C. A. Vakulskas, D. P. Dever, G. R. Rettig, R. Turk, A. M. Jacobi, M. A. Collingwood, N. M. Bode, M. S. McNeill, S. Yan, J. Camarena, C. M. Lee, S. H. Park, V. Wiebking, R. O. Bak, N. Gomez-Ospina, M. Pavel-Dinu, W. Sun, G. Bao, M. H. Porteus, M. A. Behlke, A high-fidelity Cas9 mutant delivered as a ribonucleoprotein complex enables efficient gene editing in human hematopoietic stem and progenitor cells. *Nat Med* **24**, 1216–1224 (2018).

67. S. Tiwari, A. Hontz, C. E. Terrell, P. Arumugam, M. Carmo, K. Risma, M. Jordan, P. Malik, High Level of Perforin Expression Is Required for Effective Correction of Hemophagocytic Lymphohistiocytosis. *Hum Gene Ther* **27**, 847–859 (2016).

68. T. Yasuda, T. Wirtz, B. Zhang, T. Wunderlich, M. Schmidt-Supprian, T. Sommermann, K. Rajewsky, Studying Epstein–Barr Virus Pathologies and Immune Surveillance by Reconstructing EBV Infection in Mice. *Cold Spring Harb Sym* **78**, 259–263 (2013).

69. B. Zhang, S. Kracker, T. Yasuda, S. Casola, M. Vanneman, C. Hömig-Hölzel, Z. Wang, E. Derudder, S. Li, T. Chakraborty, S. E. Cotter, S. Koyama, T. Currie, G. J. Freeman, J. L. Kutok, S. J. Rodig, G. Dranoff, K. Rajewsky, Immune Surveillance and Therapy of Lymphomas Driven by Epstein-Barr Virus Protein LMP1 in a Mouse Model. *Cell* **148**, 739–751 (2012).

70. V. T. Chu, T. Weber, B. Wefers, W. Wurst, S. Sander, K. Rajewsky, R. Kühn, Increasing the efficiency of homology-directed repair for CRISPR-Cas9-induced precise gene editing in mammalian cells. *Nat. Biotechnol.* **33**, 543–548 (2015).

71. R. Graf, X. Li, V. T. Chu, K. Rajewsky, sgRNA Sequence Motifs Blocking Efficient CRISPR/Cas9-Mediated Gene Editing. *Cell Reports* **26**, 1098-1103.e3 (2019).

72. A. R. Hersperger, G. Makedonas, M. R. Betts, Flow cytometric detection of perforin upregulation in human CD8 T cells. *Cytom Part A* **73A**, 1050–1057 (2008).

73. S. Q. Tsai, V. V. Topkar, J. K. Joung, M. J. Aryee, Open-source guideseq software for analysis of GUIDE-seq data. *Nat. Biotechnol.* **34**, 483–483 (2016).

74. M. Lebedin, *R pipeline to process and visualize the reads for GUIDE-seq according to Tsai et al., Nature Biotech, 2015* (2023; https://github.com/lebmih/R-GUIDE-seq).

75. J. Zhang, K. Kobert, T. Flouri, A. Stamatakis, PEAR: a fast and accurate Illumina Paired-End reAd mergeR. *Bioinformatics* **30**, 614–620 (2014).

76. H. Li, Minimap2: pairwise alignment for nucleotide sequences. *Bioinformatics* **34**, 3094–3100 (2018).

77. W. J. Kent, C. W. Sugnet, T. S. Furey, K. M. Roskin, T. H. Pringle, A. M. Zahler, and D. Haussler, The Human Genome Browser at UCSC. *Genome Res.* **12**, 996–1006 (2002).

78. R Core Team, *A language and environment for statistical computing.* (R Foundation for Statistical Computing, Vienna, Austria, 2020; https://www.R-project.org/).

79. S. Lin, B. T. Staahl, R. K. Alla, J. A. Doudna, Enhanced homology-directed human genome engineering by controlled timing of CRISPR/Cas9 delivery. *Elife* **3**, e04766 (2014).

80. J. A. Doudna, Addgene plasmid 69090 (RRID:Addgene_69090) *Plasmid pMJ915* (available at http://n2t.net/addgene:69090).

Acknowledgments: We thank A. Schütz and the team of the Technology Platform Protein Production and Characterization (Max-Delbrück-Center) for producing Cas9 protein and J. Doudna for the Cas9 expression plasmid pMJ915 (*79, 80*). We also thank A. Ressnerovà for her help with setting up gene targeting experiments, C. Salomon, G. Natale, and J. Pempe for their excellent technical assistance, N. Schirm and L. Rieger for animal husbandry, H.-P. Rahn of the Technology platform Flow Cytometry (Max-Delbrück-Center) for FACS-related, and Nilufar Akbari of the Service Unit Biometry (Charité - Universitätsmedizin Berlin) for statistics support.

Funding: This research was supported by the European Research Council, Advanced Gant 268921 (K.R.), the Helmholtz Association, Immunology and Inflammation ZT-0027 (K.R.), and the Berlin School of Integrative Oncology (BSIO) graduate program (PhD position) (X.L.).

Author contributions: Conceptualization: X.L., Tr.W., Ti.W., T.Y., C.K., and K.R. Methodology: X.L., Tr.W., Ti.W., M.L., T.Y. and K.d.l.R. Investigation: X.L., Tr.W., Ti.W., A.Z. and T.Y. Resources: M.L., T.S., V.T.C., K.d.l.R., J.H.S. and I.M. Visualization: X.L., C.K. and K.R. Funding acquisition: K.R. Supervision: K.R. Writing – original draft: X.L., E.L., and C.K. Writing – review & editing: C.K. and K.R. with input from X.L.

Competing interests: Tr.W. is currently a Pfizer Inc. employee. The remaining authors declare that they have no competing interests.

Data and materials availability: Mouse and human HDR templates for perforin targeting were cloned into the publicly available pDonor backbone vector and deposited to Addgene (#209073, #209074, #209075, #20906). GUIDE-seq sequencing data have been deposited in the National Center for Biotechnology Information (NCBI) Sequence Read Archive (SRA) database, accession PRJNA1016463. All other data are available in the main text, the supplementary materials and in data file S2.

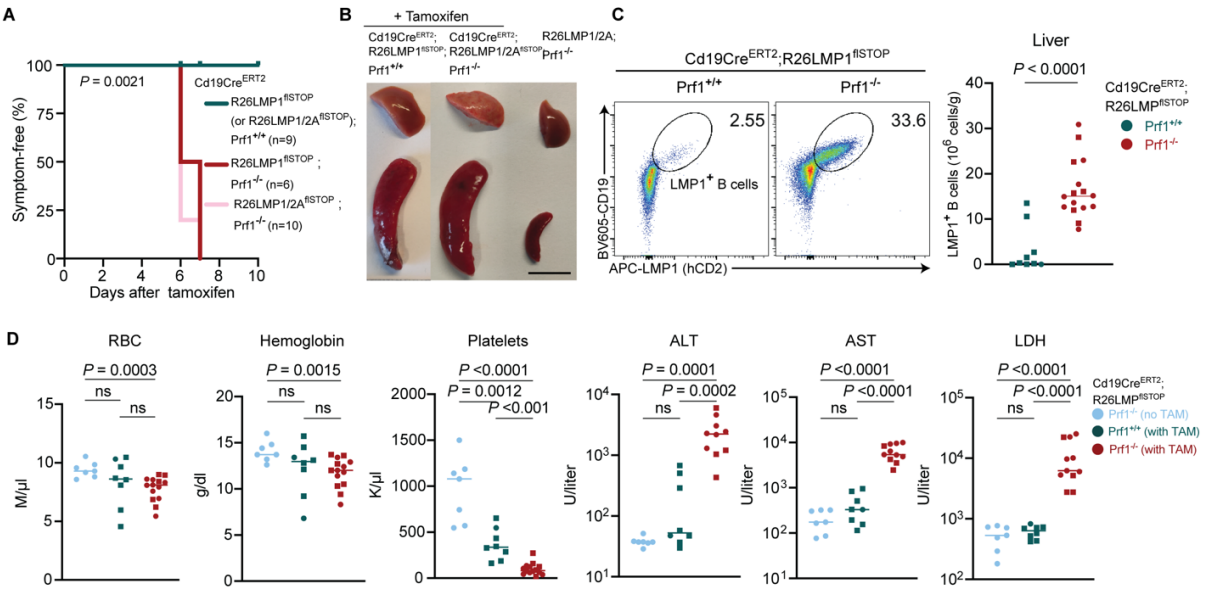

Fig. 1. A mouse model for fatal EBV infection recapitulates key features of FHL2. In perforin-deficient mice, B-cell specific induction of EBV genes LMP1 or LMP1 and 2A by tamoxifen leads to a rapid disease onset and fulminant, systemic hyperinflammation resembling FHL2 (*25*). (**A**) Graph depicting Kaplan-Meier curves of symptom-free survival of perforin-1–deficient and perforin-1–expressing control mice. Significance was calculated with a log-rank test (Mantel–Cox (conservative): $P = 0.0021$ for three groups, and $P = 0.002$ (R26LMP1^{flSTOP};*Prf1*$^{-/-}$) and $P < 0.0001$ (R26LMP1/2A^{flSTOP};*Prf1*$^{-/-}$) for pairwise comparisons). Upon induction of LMP-expression by tamoxifen, the animals were closely monitored by visual observation for signs of end-stage disease (strongly reduced activity, hunched posture, and ungroomed fur) and sacrificed when they showed all three symptoms combined (humane endpoint). End-stage symptoms developed within 1 week. Symptom-free mice appeared normal and showed no signs of disease. Results are pooled from four independent experiments for a total of 16 *Prf1*-deficient and 9 *Prf1*-expressing control mice. (**B**) Representative pieces of livers (upper row) and spleens (lower row) 6 days after tamoxifen administration. Livers from perforin-deficient mice appear whitish pale from leukocyte infiltrates and spleens are grossly enlarged. Scale bar, 1 cm. (**C**) LMP1$^+$ B cell numbers in the liver are greatly elevated in perforin-1–deficient mice 6 to 7 days after tamoxifen administration. Left: representative flow cytometry plots. LMP1$^+$ B cells were gated on live cells, and identified as hCD2-reporter$^+$, CD19$^+$, or B220$^+$ B cells. Right: LMP1$^+$ B cell numbers (10^6 cells/gram liver tissue). Each symbol represents one mouse and horizontal lines indicate medians. Results are pooled from four independent experiments for a total of 16 *Prf1*-deficient and 9 *Prf1*-expressing control mice (A and C). (**D**) Tamoxifen-treated, perforin-1–deficient mice show reduced red blood cell (RBC) counts, hemoglobulin levels, and platelet counts, all indicative of cytopenia, as well as increased tissue damage as indicated by various serum markers 6-10 days after tamoxifen treatment. Each dot represents one mouse. Horizontal lines indicate medians. Results are pooled from four independent experiments for a total of 11 to 14 *Prf1*-deficient and 8 *Prf1*-expressing control mice. For comparison, 7 *Prf1*-deficient mice without tamoxifen treatment are shown as non-

induced controls (no LMP1 induction). Symbols indicate genotype: square (*Cd19*-Cre^{ERT2};R26LMP1^{flSTOP};*Prf1*$^{-/-}$), round (*Cd19*-Cre^{ERT2};R26LMP1/LMP2A^{flSTOP};*Prf1*$^{-/-}$). (C and D) Significance was calculated with a two-tailed Mann-Whitney test. ALT, alanine aminotransferase; AST, aspartate aminotransferase; LDH, lactate dehydrogenase; M, million; U, unit.

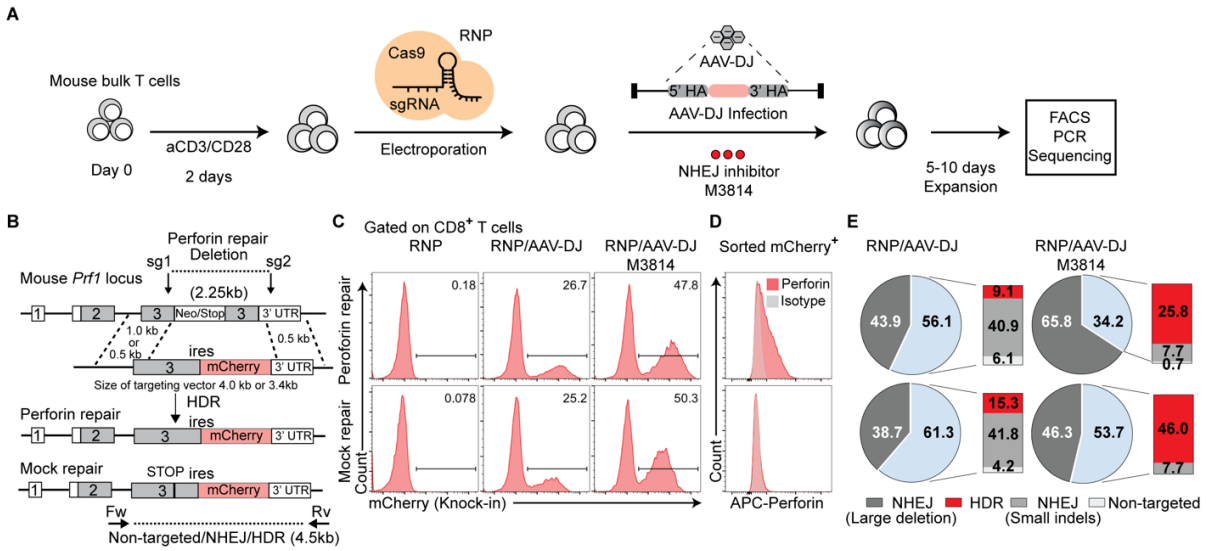

Fig. 2. Highly efficient CRISPR/Cas9 repair of the *Prf1* gene in mouse bulk T cells. (**A**) Ex vivo CRISPR–Cas9 gene repair strategy for primary mouse T cells from *Prf1*$^{-/-}$ mice, using recombinant adeno-associated virus (AAV) vectors to provide single-stranded DNA repair templates with homology arms (HA). AAV-DJ was used for mouse cells. M3814—a small molecule inhibitor of non-homologous end joining (NHEJ)—was added to favor homology-directed repair (HDR). (**B** to **E**) Knock-in efficiency for the mouse perforin gene locus: (B) Targeting strategy. Gene locus containing a Neo-Stop-Cassette (upper line), donor template (middle line) and targeted loci (lower two lines). (C) Percentage of targeted bulk T cells (mCherry^{+}) determined by flow cytometry after the indicated treatments with Cas9–gRNA ribonucleoprotein (RNP) complexes. Results are representative of at least four independent experiments. (D) Intracellular perforin staining of repaired sorted mCherry^{+} CD8 T cells. Results correspond to one of two independent experiments. (E) Percentage of targeted alleles determined by gel electrophoresis (pie chart) and by sequencing. Upper row: Perforin repair; lower row: Mock repair. Results correspond to one of two independent experiments each.

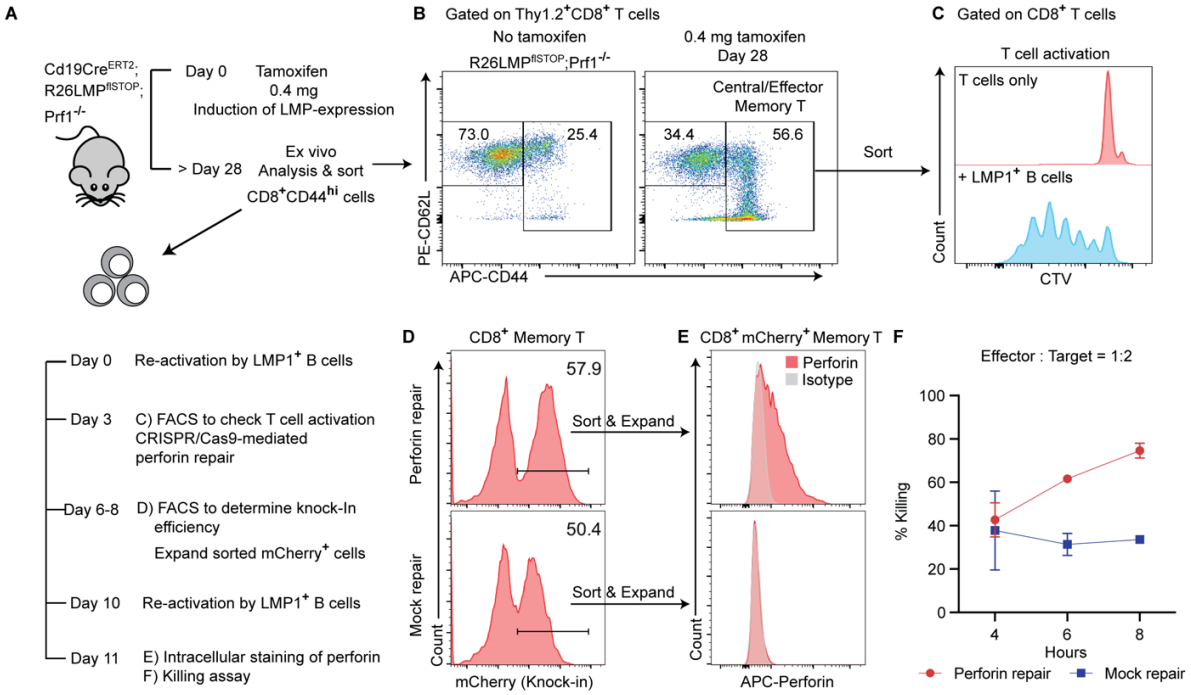

Fig. 3. Repair of perforin-1–deficient, LMP1-specific mouse memory T cells. (**A**) Experimental setup. (**B**) Ex vivo flow cytometry analysis of splenocytes. Result corresponds to one of two independent experiments and is representative of four mice in total (0.4 mg tamoxifen, Day 28 to 60). Control corresponds to one representative of three *Prf1* -deficient mice (no tamoxifen). (**C**) Activation of sorted CD44^{hi} CD8 memory T cells by LMP1-expressing B cell line 2726L. Results are representative of four independent experiments. (**D**) Percentage of targeted memory T cells (mCherry^{+}) and (**E**) intracellular perforin-1 staining of sorted mCherry^{+} CD8 memory T cells. Results correspond to one of three (D) or two (E) independent experiments. (**F**) Killing of LMP1-expressing B cell line 2726L by perforin-repaired or mock-repaired memory T cells. Results correspond to means ± s. d. of triplicate measurements for one of two independent experiments.

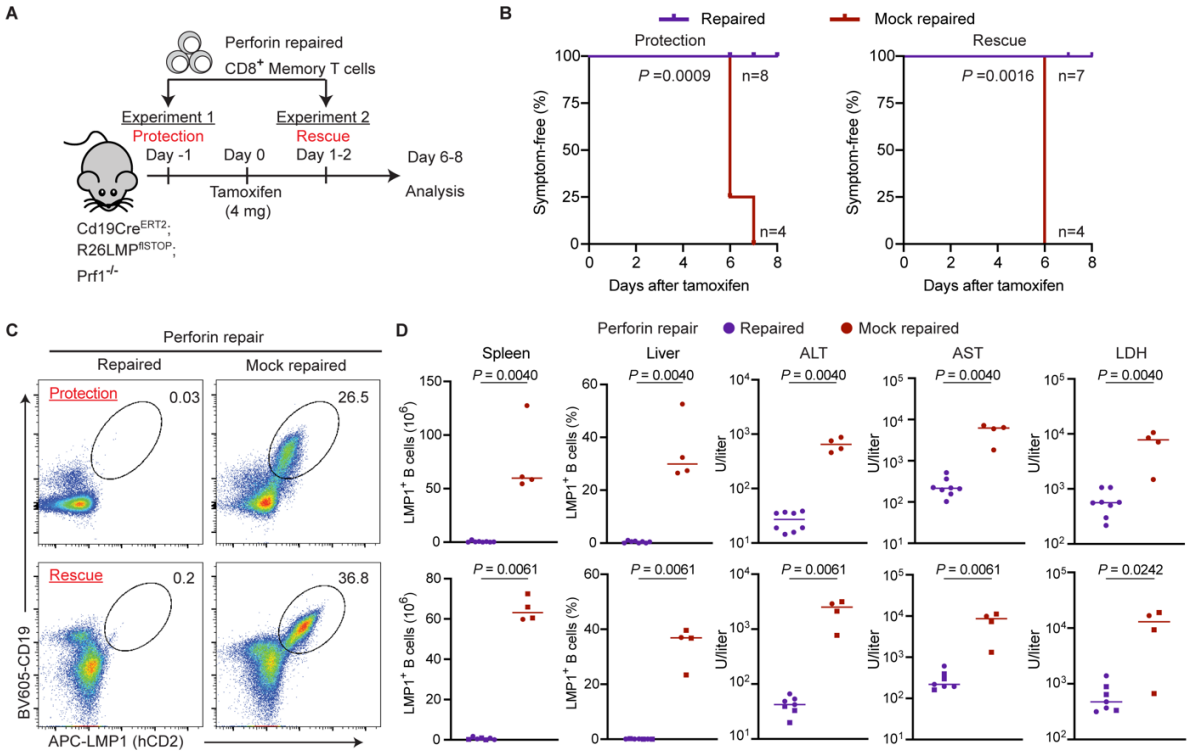

Fig. 4. Repaired memory T cells protect perforin-1–deficient mice from hyperinflammation. (**A**) Scheme of T cell therapy experiments in a mouse model of tamoxifen-inducible familial FHL2 (*25*) (see Fig. 1). (**B**) Graph depicting Kaplan-Meier curves of symptom-free survival of perforin-1– deficient mice treated with perforin-repaired or mock-repaired T cells (log-rank test (Mantel–Cox (conservative)). Upon induction of LMP-expression by tamoxifen, mice were closely monitored by visual observation for signs of end-stage disease (strongly reduced activity, hunched posture, ungroomed fur) and sacrificed when they showed all three symptoms (humane endpoint). Symptom-free mice appeared normal and showed no sign of disease. Perforin-repaired memory T cells conferred full protection (left) or full rescue (right) from disease symptoms. (**C**) Flow cytometry analysis to detect infiltrating LMP1$^+$ B cells in liver (gated on live cells, identified as hCD2-reporter$^+$, CD19$^+$, or B220$^+$ B cells) in perforin-1–deficient mice which received repaired memory T cells before ("Protection", upper panel) or after ("Rescue", lower panel) induction of LMP by tamoxifen. Results show one representative mouse each per genotype and condition. (**D**) Repaired memory T cells can eliminate LMP1$^+$ B cells in spleen and liver and thereby prevent liver damage due to hyperinflammation ("Protection", upper panels; "Rescue", lower panels). Numbers of LMP1$^+$ B cells were determined by flow cytometry and serum markers measured 6 to 10 days after induction of LMP-expression by tamoxifen. Each dot represents one mouse. Horizontal lines indicate medians and symbols indicate genotype: square (*Cd19*-Cre^{ERT2};R26LMP1^{flSTOP};*Prf1*$^{-/-}$), round (*Cd19*-Cre^{ERT2};R26LMP1/LMP2A^{flSTOP};*Prf1*$^{-/-}$). (B to D) Results are pooled from two independent experiments for a total of 8 or 7 *Prf1*-deficient mice treated with repaired T cells and 4 *Prf1*-deficient mice treated with mock repaired T cells. Significance was calculated with a

two-tailed Mann-Whitney test. ALT, alanine aminotransferase; AST, aspartate aminotransferase, LDH, lactate dehydrogenase, U, unit.

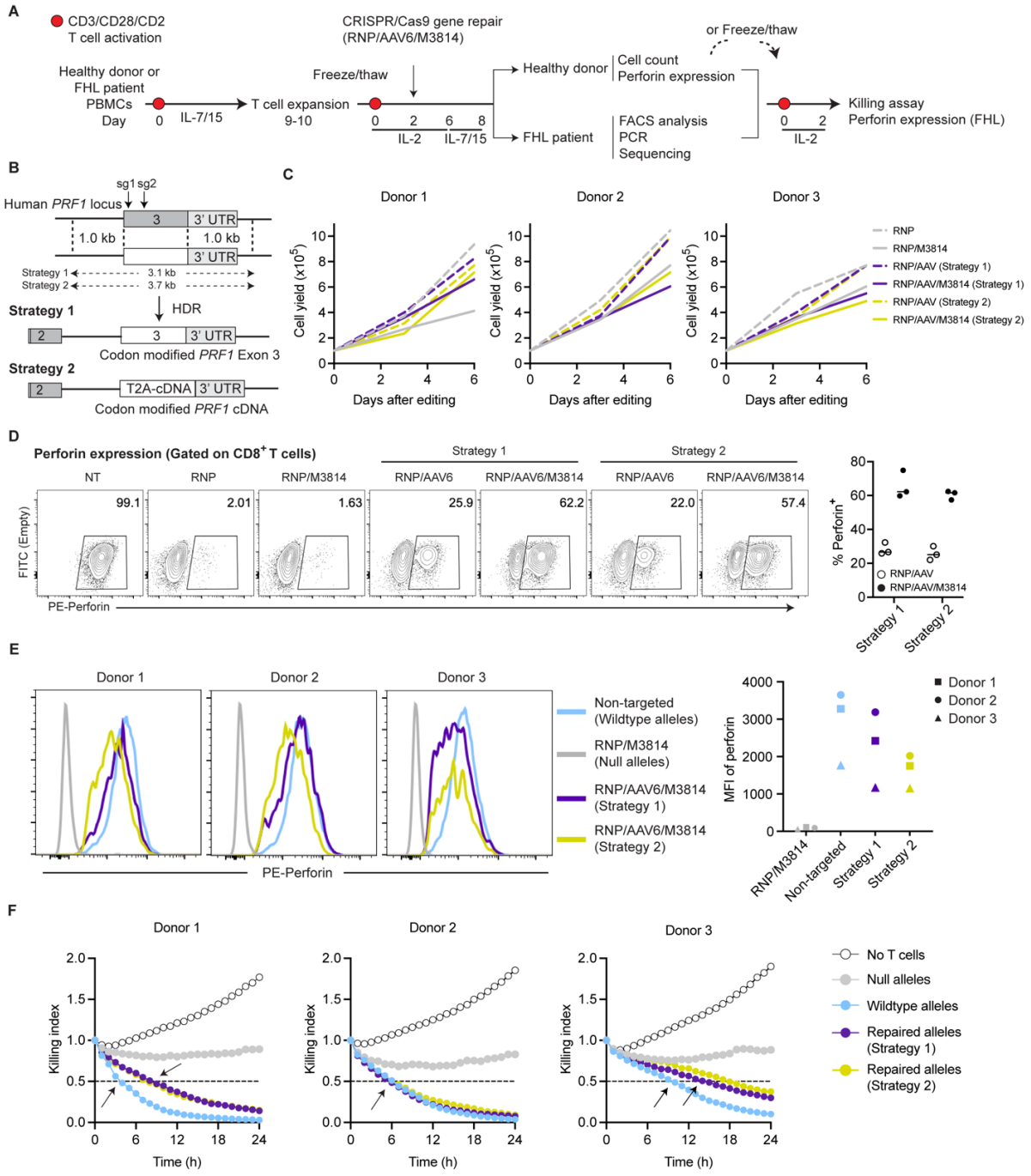

Fig. 5. Efficiency of *PRF1* gene repair strategies in T cells from healthy donors. (**A**) Experimental workflow schematic. (**B**) Gene repair strategies for the two patient alleles which carry distinct mutations in exon 3 of the *PRF1* gene. Strategy 1 replaces exon 3 with a wildtype exon, strategy 2 with a complete *PRF1* coding sequence (*PRF1* cDNA preceded by a T2A self-cleaving peptide). (**C**) Expansion of edited cells over time, starting from 10^5 input T cells. Data are from one experiment per donor. (**D**) Intracellular perforin staining with monoclonal antibody

B-D48 (*72*) of healthy donor T cells analyzed by flow cytometry after the indicated treatments. Left: Flow cytometry plots depict data from one representative donor of three donors per treatment. Right: Frequency of perforin-expressing, CD8 T cells after targeting of *PRF1* alleles by the indicated treatments. Each dot represents one independent experiment per donor for three donors per treatment. Horizontal lines indicate medians (**E**) Intracellular perforin protein levels before and after gene editing, measured by flow cytometry. T cells were gated on perforin-1^{+} cells, except the knock-out sample which did not receive the AAV6 repair template (gray line, RNP/M3814). Left: Flow cytometry. Right: Mean fluorescence intensities (MFI) of perforin. Data are from one independent experiment per donor, for three donors. (**F**) Cytotoxic activity in edited T cells. *PRF1* knock-out abolished and *PRF1* repair restored efficient killing of mCherry-expressing target cells (Burkitt lymphoma BJAB cells). Arrow indicates the respective time points of 50% killing of target cells. Data are from one independent experiment per donor, for three donors.

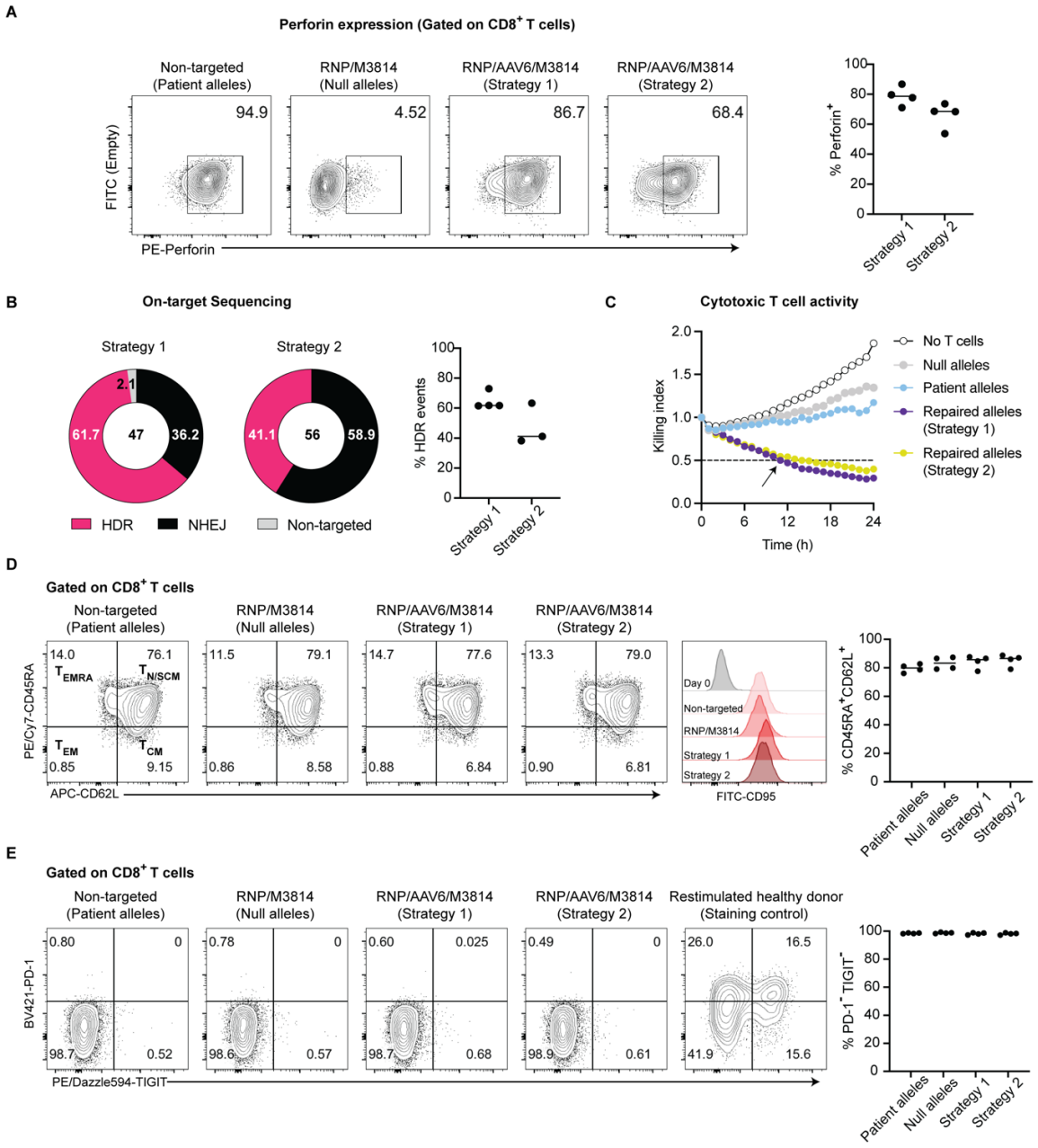

Fig. 6. Efficient repair of perforin mutations in T cells from an FHL2 patient. (**A**) Intracellular perforin staining with monoclonal antibody B-D48 (*72*) of patient T cells analyzed by flow cytometry after the indicated treatments. Left: Flow cytometry plots are representative of four independent experiments. Right: Frequency of perforin-1–expressing CD8 T cells after repairing mutated patient *PRF1* alleles by RNP/AAV6/M3814 treatment. Each dot represents one independent experiment (n=4). Horizontal lines indicate medians. (**B**) Percentage of targeted alleles as determined by PCR amplification, cloning and sequencing after RNP/AAV6/M3814 treatment. Left: Pie charts shows results representative of four (strategy 1) and three (strategy 2) independent experiments. Right: Quantification of HDR events. Each dot represents one

independent experiment. Horizontal lines indicate medians. (**C**) Restored, cytotoxic activity in repaired patient T cells. *PRF1* repaired T cells showed faster, more efficient killing of mCherry-expressing target cells (Burkitt lymphoma BJAB cells). Arrow indicates the respective time points of 50% killing of target cells. Note that patient T cells had residual killing activity that disappeared upon engineering true *PRF1* null alleles. Data are representative of four independent experiments. (**D**) Representative phenotypes by flow cytometry of repaired FHL2 patient–derived CD8 T cells after the indicated treatments. $CD45RA^+CD62L^+$ T cells were almost exclusively $CD95^+$, differentiating them from naïve T cells and identifying them as T memory stem cell-like. (**E**) Repaired CD8 T cells did not express the T cell exhaustion markers PD-1 and TIGIT. (D and E) Left: Flow cytometry plots representative of four independent experiments. Right: Quantification of phenotyped T cells. Each dot represents one independent experiment (n=4). Horizontal lines indicate medians. T_{EMRA}, effector memory T cells re-expressing CD45RA; T_{EM}, effector memory T cells; T_N, naïve T cells; T_{SCM}, T memory stem cells; T_{CM}, central memory T cells.

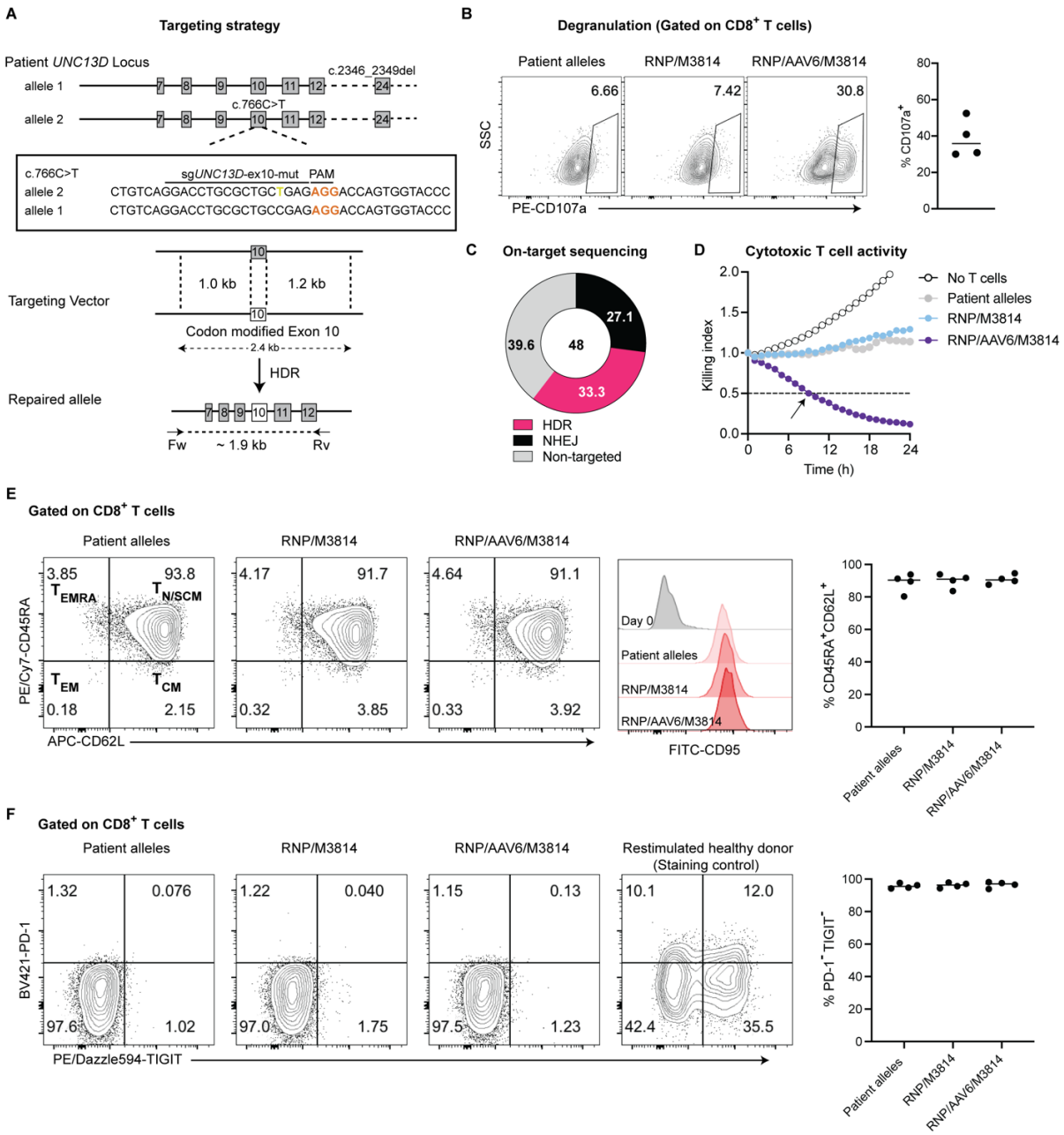

Fig. 7. Allele-specific repair of an *UNC13D* mutation in T cells from an FHL3 patient. (**A**) Gene repair strategy for one of two mutated alleles in the patient *UNC13D* locus. PAM sequences are indicated in red. The sgRNA sgUNC13D-ex10-mut targets specifically the allele mutated in exon 10. Positions of PCR primers are indicated. (**B**) Restored degranulation capacity as measured by increased CD107a staining after repair of one allele in patient T cells. Left: Flow cytometry plots are representative of four independent experiments. Right: Quantification of degranulation after RNP/AAV6/M3814 treatment. Each dot represents one independent experiment (n=4). Horizontal lines indicate medians. (**C**) Percentage of targeted alleles determined by PCR amplification, cloning and sequencing after RNP/AAV6/M3814 treatment

(n=4) (see table S2). Results correspond to one of four independent experiments. (**D**) Restored cytotoxic activity in repaired patient T cells. Allele-specific repair of *UNC13D* was sufficient restore cytotoxic activity as measured by killing of mCherry-expressing BJAB cells. The arrow indicates the time point of 50% target cell killing. Results correspond to (C) and are representative of four independent experiments. (**E**) Representative phenotypes by flow cytometry of repaired, FHL3 patient-derived CD8 T cells after the indicated treatments. $CD45RA^{+}CD62L^{+}$ T cells were almost exclusively CD95-positive, distinguishing them from naïve T cells and identifying them as T memory stem cell-like. (**F**) Repaired CD8 T cells did not express the T cell exhaustion markers PD-1 and TIGIT. (E and F) Left: Flow cytometry plots representative of four independent experiments. Right: Quantification of of phenotyped T cells. Each dot represents one independent experiment (n=4). Horizontal lines indicate medians. T_{EMRA}, effector memory T cells re-expressing CD45RA; T_{EM}, effector memory T cells; T_N, naïve T cells; T_{SCM}, T memory stem cells; T_{CM}, central memory T cells.

Supplementary Materials for

Precise gene repair in autologous memory T cells to treat familial hemophagocytic lymphohistiocytosis

Xun Li, Tristan Wirtz, Timm Weber, Mikhail Lebedin, Elijah D. Lowenstein, Thomas Sommermann, Andreas Zach, Tomoharu Yasuda, Kathrin de la Rosa, Van Trung Chu, Johannes H. Schulte, Ingo Müller, Christine Kocks, Klaus Rajewsky

*Corresponding author. Email: klaus.rajewsky@mdc-berlin.de.

This PDF file includes:

Other Supplementary Materials for this manuscript include the following:

SUPPLEMENTARY TEXT

Clinical information on the FHL2 patient (Fig. 6 and figs. S3 and S4)

The patient was delivered in the 40th week of pregnancy by primary caesarian section to non-consanguineous healthy parents. Due to elevated infectious parameters and respiratory adaption problems, he received postnatally 1 week of intravenous antibiotic treatment. Platelets were decreased, but could successfully be substituted excluding an allo-immune thrombocytopenia. He was discharged from neonatology on his 16th day of life. Only 12 days later, he was re-admitted with feeding problems, weakness, pallor, and massive hepatosplenomegaly. Pathologic laboratory results included Hb 4.8 g/dl, thrombocytopenia 25.000/nl, CrP 67.4 mg/L, sIL-2R 15.921 U/ml, ferritin 1882 µl, Fibrinogen was 2.0 g/l, triglycerides 173 mg/dl, and EBV-PCR neg. Bone marrow aspiration showed very active hemophagocytosis. The diagnosis of FHL was finally corroborated based on compound heterozygous loss of function mutations in the *PRF1* gene (c.853-855del AAG(285delK) and c.1349C>T(T450M), which were also found separately in each parent. The patient was treated with dexamethasone and weekly etoposide pulses leading to a rapid improvement of his clinical condition and normalization of inflammatory lab parameters. At the age of 4 months, the patient underwent allogeneic bone marrow transplantation from a 9/10 HLA-compatible unrelated donor. With a follow-up of 6 years, the child developed adequately to age and is disease-free despite low donor chimerism of 21% in the T cell compartment. The subject's blood sample was frozen under cyclosporine A and just off treatment with dexamethasone. Informed consent was obtained from the legal guardians of the patient and the IRB of the Hamburg State Medical Association approved the study (ID PV5777). (Provided by I. Müller)

Clinical information on the FHL3 patient (Fig. 7 and fig. S7)

The male baby was admitted to a hospital at an age of 32 days for a failure to thrive and icterus. The patient developed fever, increasing inflammation, thrombocytopenia, anemia, and hepatosplenomegaly. Laboratory findings included sIL2R 65.742 IU/ml, bilirubin 4.68 mg/dl, ferritin 5.938 µg/l, triglycerides 204 mg/dl, fibrinogen 1.34 g/l, PCT 1.86 µg/l, and LDH 565 U/l. He was diagnosed with HLH, fulfilling seven of eight diagnostic criteria for primary HLH (*12*). The diagnosis of primary HLH was genetically confirmed by compound heterozygous mutation in UNC13B: Mutation 1: c.766C>T p.Arg256* (Exon 10) and Mutation 2: c2346_2349del p.Arg782Serfs*12 (Exon 24). The patient was treated according to the HLH-2004 protocol (*12*). Treatment included dexamethasone, VP16 and Cyclosporine A. With this treatment, the clinical condition of the patient improved, and the inflammation decreased. During this treatment, blood samples for experiments in the Rajewsky lab were collected. The patient underwent bone marrow transplantation from an 12/12 HLA-identical matched unrelated donor. Because of decreased donor chimerism, the patient had to undergo retransplantation approximately 5 months after the initial transplantation. More than 4 years after the transplantation, the patient has a stable, donor-predominant chimerism, is healthy without any signs or symptoms of HLH, has no late effects of transplantations, and is developing well. Written informed consent was obtained from the legal guardians of the patient and the IRB/Ethics Committee of Charité Universitätsmedizin Berlin approved the study [approval no. EA2/144/15]. (Provided by J. H. Schulte)

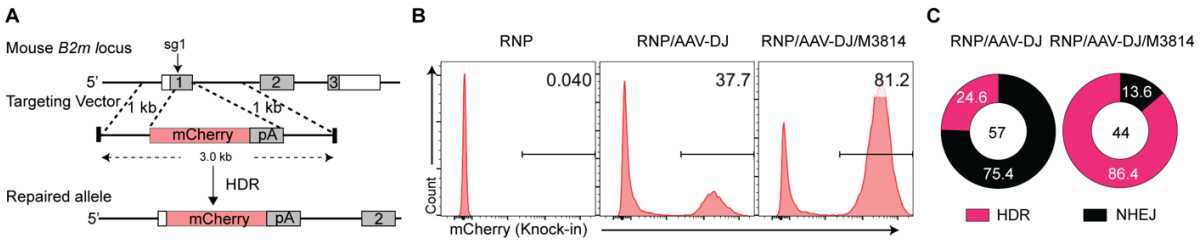

Fig. S1. Highly efficient CRISPR/Cas9-mediated reporter insertion into the *B2m* locus of mouse T cells. (**A**) Targeting strategy. Gene locus (upper line), targeting vector (middle line) and targeted locus (lower line). (**B** and **C**) Knock-in efficiency for the mouse *B2m* locus: (B) Percentage of targeted T cells (mCherry^{+}) determined by flow cytometry after the indicated treatments with Cas9 ribonucleoprotein complexes (RNP) and AAV. Results are representative of four independent experiments. (C) Percentage of targeted alleles determined by PCR, cloning and sequencing. Results correspond to one experiment per treatment condition.

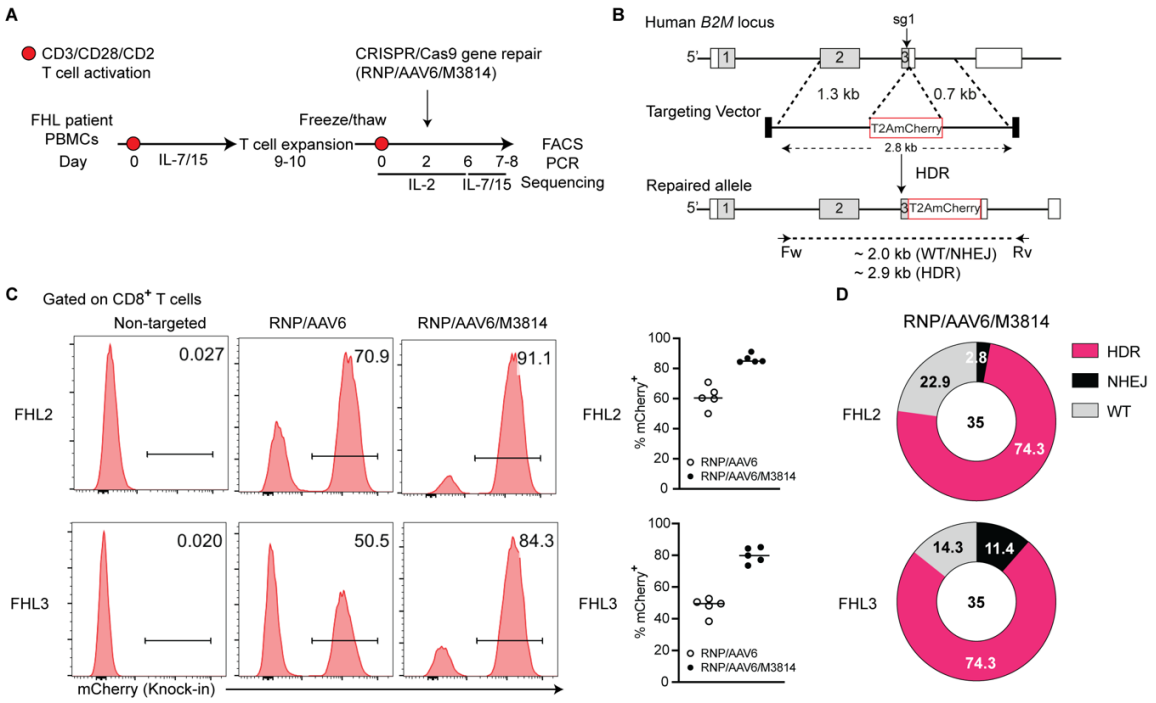

Fig S2. Highly efficient gene repair of *B2M* in T cells from one FHL2 and one FHL3 patient. (**A**) Experimental workflow: expansion of FHL T cells and insertion of T2A-mCherry reporter into the *B2M* locus in T cells from an FHL2 and an FHL3 patient. (**B**) Targeting strategy. Gene locus (upper line), targeting vector (middle line) and targeted locus (lower line), with PCR primers for amplification of wild-type (WT)/NHEJ and HDR sequences indicated. (**C**) Left: Percentage of targeted T cells (mCherry^{+}) determined by flow cytometry after the indicated treatments. Results are representative of five independent experiments per patient and per condition. Right: Quantification of mCherry^{+} T cells after targeting the *B2M* locus with indicated treatments. Each dot represents one independent experiment (n=5). Horizontal lines indicate medians. (**D**) Percentage of targeted alleles as determined by PCR amplification, cloning and sequencing. Results correspond to one experiment per patient.

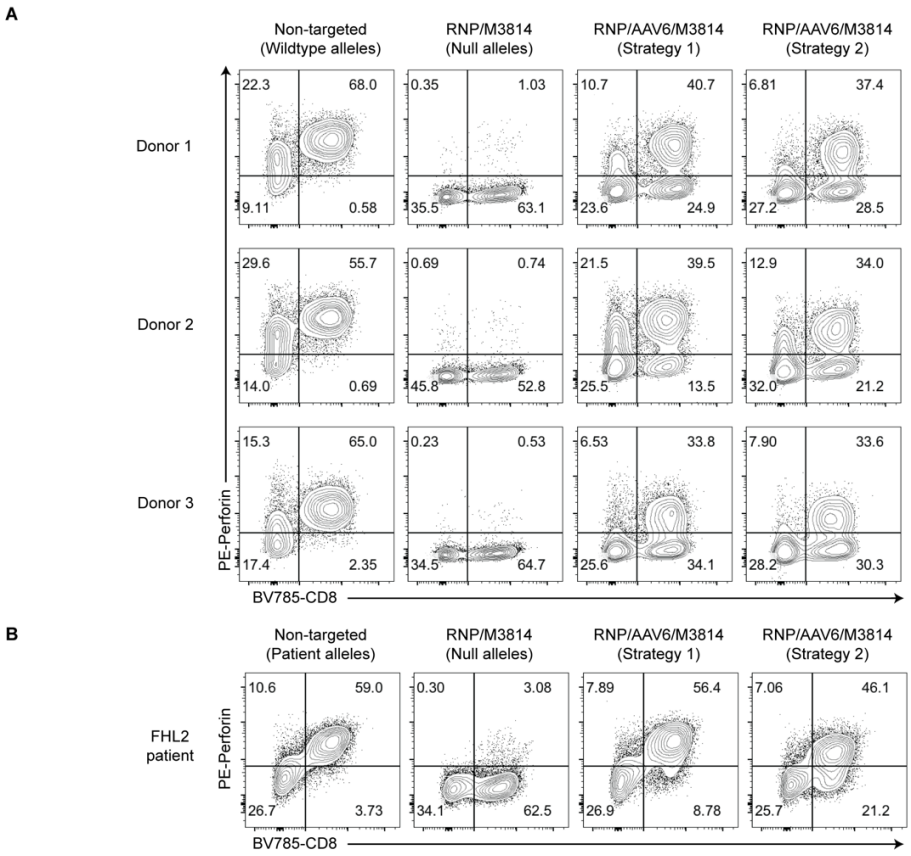

Fig. S3. CD8 T cells are the main perforin-expressing T cell subpopulation after gene editing. PBMCs were cultured, and T cells activated, expanded and edited as schematically shown in Fig. 5A. For intracellular perforin protein detection, reactivated T cells were stimulated with PMA and ionomycin in presence of brefeldin A for 6 hours, fixed and stained, and analyzed by flow cytometry. Cells were gated on live T cells. (**A**) Healthy donor T cells with the indicated gene editing treatments. Results are from one independent experiment per donor, for three donors. (**B**) FHL2 patient T cells with the indicated gene editing treatments. Results are representative of four independent experiments. Note that in non-targeted FHL2 patient T cells non-functional perforin protein is detected, since the c.1349C>T(T450M) missense mutation is known to generate an altered perforin with impaired proteolytic maturation.

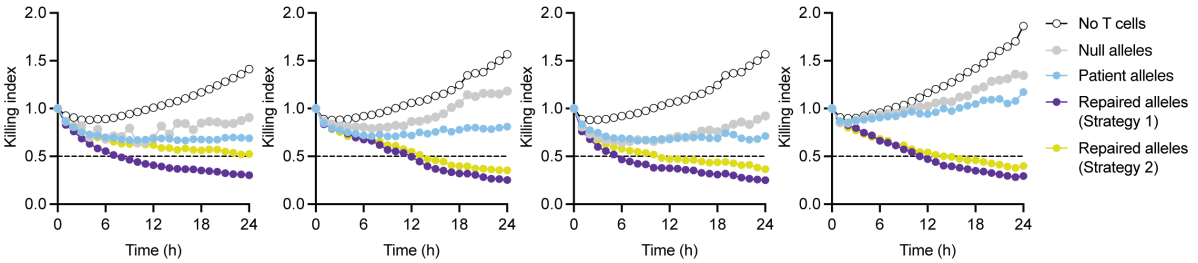

Fig. S4. Restored cytotoxic activity in repaired T cells from the FHL2 patient. From left to right: Individual, independent biological repeat experiments corresponding to Fig. 6C. The fourth panel, shown for comparison, is identical to Fig. 6C.

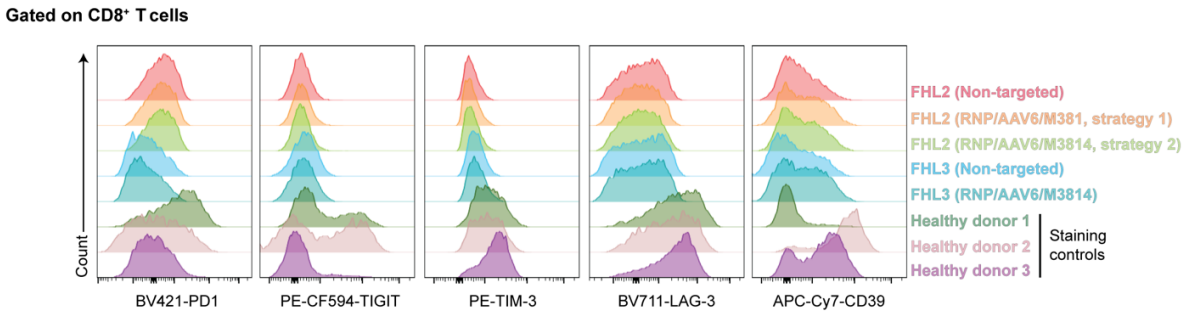

Fig. S5. Repaired FHL patient CD8 T cells do not overexpress T cell exhaustion markers. FHL patient PBMCs were cultured and T cells activated, expanded and edited as schematically shown in Fig. 5A. Six days after gene editing, cells were analyzed by flow cytometry with pregating on CD8 T cells. Displayed are representative histograms for the expression of inhibitory receptors linked to T cell exhaustion (PD-1, TIGIT, TIM-3, LAG-3, and CD39) after the indicated gene editing treatments. Results are representative of four independent experiments. As antibody staining controls, we used CD8 T cells from healthy donors that were restimulated with CD3/CD28/CD2 plus human IL-2 for 2 days.

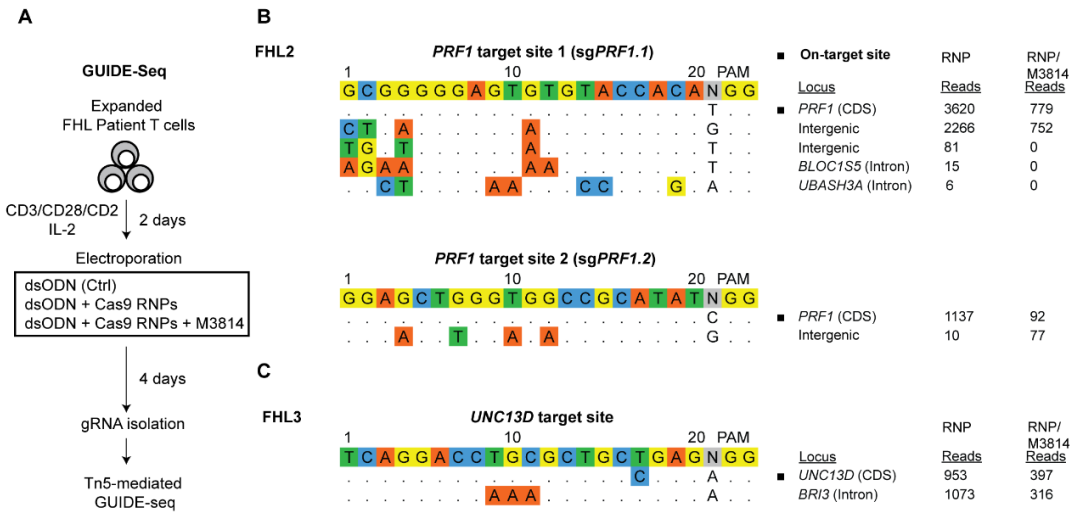

Fig. S6. Genome-wide off-target analysis by GUIDE-seq (**A**) Experimental scheme for the GUIDE-seq experiments. FHL patient PBMCs were cultured, and T cells activated, expanded and edited as indicated. Four days after gene editing, genomic DNA was extracted and processed for Tn5-mediated GUIDE-seq. (**B**) Detected on-target (black square) and off-target sequences for the indicated treatments are shown with the respective mismatches to the protospacer sequence. The displayed results are based on pooled data from three independent repeat experiments per patient. For exact locations of off-target sites see Data S1.

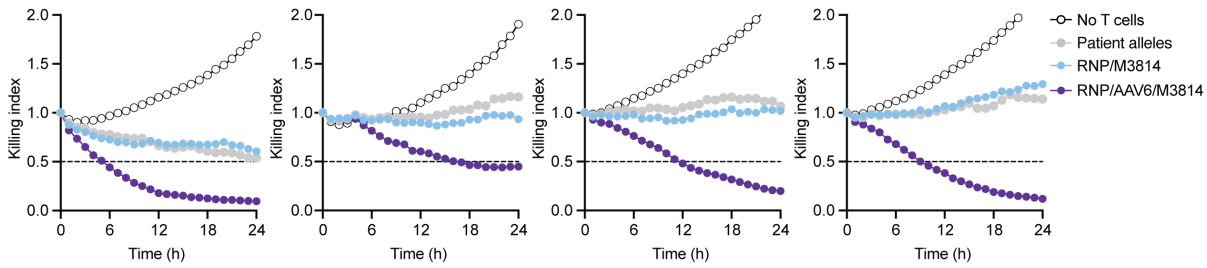

Fig. S7. Restored cytotoxic activity in repaired T cells from the FHL3 patient. From left to right: Individual, independent biological repeat experiments corresponding to Fig. 7D. The fourth panel, shown for comparison, is identical to Fig. 7D.

Table S1. Knock-in efficiencies measured by flow cytometry of targeted T cells.

Species	Figure	Locus	Repair strategy	Number (n) (indep. exp.)	% of repaired T cells (medians)
Mouse	Fig. 2C	Perforin repair	RNP/AAV	6	27.4
			RNP/AAV/M3814	6	49.05
		Mock repair	RNP/AAV	4	28.4
			RNP/AAV/M3814	4	52.45
Mouse	Fig. 3D	Perforin repair	RNP/AAV	3	35.4
			RNP/AAV/M3814	3	48.7
		Mock repair	RNP/AAV	3	37.4
			RNP/AAV/M3814	3	50.4
Mouse	fig. S1B	B2m	RNP/AAV	4	38.05
			RNP/AAV/M3814	4	79.4
Human	Fig. 5D	PRF1	RNP/AAV Strategy 1	3	26.6
			RNP/AAV/M3814 Strategy 1	3	62.2
			RNP/AAV Strategy 2	3	25.1
			RNP/AAV/M3814 Strategy 2	3	61.6
Human	Fig. 6A	PRF1	RNP/AAV/M3814 Strategy 1 (Two sgRNAs)	4	78.65
			RNP/AAV/M3814 Strategy 1 (One sgRNA: sg*PRF1.2*)	3	51.2
			RNP/AAV/M3814 Strategy 2 (Two sgRNAs)	4	68.5
			RNP/AAV/M3814 Strategy 2 (One sgRNA: sg*PRF1.2*)	2	47.0, 51.2
Human	Fig. 7B	UNC13D	RNP/AAV/M3814	4	35.85
Human	fig. S2C	B2M (FHL2)	RNP/AAV	5	60.4
			RNP/AAV/M3814	5	84.9
		B2M (FHL3)	RNP/AAV	5	49.5
			RNP/AAV/M3814	5	79.9

The percentage of repaired T cells in the presence or absence of NHEJ inhibitor M3814 is shown as medians of the indicated number (n) of experiments. See also the respective figure legends.

Table S2. Knock-in efficiencies measured by sequencing of targeted alleles.

Species	Figure	Locus	Repair strategy	% HDR	% NHEJ		% Non-targeted
					Large deletion	Small indels	
Mouse	Fig. 2E	Perforin repair	RNP/AAV	9.1	43.9	40.9	6.1
			RNP/AAV/M3814	25.8	65.8	7.7	0.7
		Mock repair	RNP/AAV	15.3	38.7	41.8	4.2
			RNP/AAV/M3814	46.0	46.3	7.7	0
		Perforin repair	RNP/AAV	19.9	36.3	41.8	2.0
			RNP/AAV/M3814	28.9	66.9	4.1	0
		Mock repair	RNP/AAV	28.9	36.3	30.9	3.9
			RNP/AAV/M3814	59.2	30.0	8.1	2.7
Mouse	fig. S1C	B2m	RNP/AAV	24.6	75.4		0
			RNP/AAV/M3814	86.4	13.6		0
Human	Fig. 6B	PRF1	RNP/AAV/M3814 Strategy 1	61.8	35.3		2.9
				73.0	27.0		0
				61.5	35.9		2.6
				61.7	36.2		2.1
			RNP/AAV/M3814 Strategy 2	38.2	58.8		2.9
				63.3	23.3		13.3
				41.1	58.9		0
Human	Fig. 7C	UNC13D	RNP/AAV/M3814	69.0	10.3		20.7
				40.0	24.0		36.0
				58.3	8.3		33.3
				33.3	27.1		39.6
Human	fig. S2D	B2M (FHL2)	RNP/AAV/M3814	74.3	2.8		22.9
		B2M (FHL3)	RNP/AAV/M3814	74.3	11.4		14.3

The percentage of HDR, NHEJ, or non-targeted sequences in T cells that were targeted in the presence or absence of NHEJ inhibitor M3814 is shown. Each row corresponds to one independent experiment. See also the respective figure legends.

Table S3. The nucleotide sequence of expression-optimized *PRF1* exon 3.

CTTTCACGTGGTGCACACACCTCCACTGCACCCCGATTTCAAGAGAGCCCTGGGAGATCTGCCCCAC
CACTTCAATGCTAGCACACAGCCTGCCTACCTGAGACTGATCAGCAACTACGGCACCCACTTCATCA
GAGCCGTGGAACTCGGAGGCAGAATCTCTGCCCTGACAGCCCTGAGAACATGCGAACTGGCTCTGG
AAGGCCTGACCGACAACGAGGTGGAAGATTGTCTGACCGTGGAAGCCCAAGTGAACATCGGCATCC
ACGGATCTATCTCTGCCGAGGCCAAGGCCTGCGAGGAAAAGAAAAAGAAACACAAGATGACCGCC
AGCTTCCACCAGACCTACCGGGAAAGACACTCTGAGGTTGTCGGCGGCCACCACACCAGCATCAAT
GACCTGCTGTTTGGCATCCAAGCTGGCCCTGAGCAGTACAGCGCTTGGGTTAACTCTCTGCCTGGCT
CTCCTGGCCTGGTGGATTACACACTGGAACCTCTGCACGTGCTGCTGGACTCTCAGGATCCTAGAAG
AGAGGCTCTGAGAAGGGCTCTGAGCCAGTACCTGACCGATAGAGCTAGATGGCGGGACTGCAGCA
GACCTTGTCCTCCTGGTAGACAGAAGTCCCCTAGAGATCCTTGCCAGTGCGTGTGTCACGGAAGCGC
CGTTACCACACAGGATTGCTGCCCAAGACAGAGAGGACTGGCCCAGCTGGAAGTGACCTTTATTCA
GGCTTGGGGCCTGTGGGGCGATTGGTTTACAGCCACAGATGCCTACGTGAAGCTGTTCTTTGGCGGC
CAAGAGCTGAGAACCAGCACCGTGTGGGACAACAACAACCCCATTTGGAGCGTGCGGCTGGATTTC
GGAGATGTCTTGCTTGCAACAGGCGGCCCTCTGAGACTGCAAGTGTGGGATCAAGACAGCGGCAGG
GACGATGATCTGCTGGGCACATGTGATCAGGCCCCTAAGTCTGGAAGCCACGAAGTGCGGTGCAAC
CTGAATCACGGCCACCTGAAGTTCAGATACCACGCCAGATGTCTGCCTCACCTCGGCGGAGGCACA
TGTCTGGATTATGTGCCTCAGATGCTGCTCGGCGAGCCTCCTGGAAATAGAAGCGGAGCTGTGTGGT
GA

Table S4. The nucleotide sequence of expression-optimized *PRF1* T2A-cDNA.

T**tccGGCAGCGGC**gagggcagaggaagtctgctaacatgcggtgacgtggaggagaatcccggccct**ATG**GCTGCTAGACTGCTGC
TGCTGGGAATCCTGCTGCTTCTGCTTCCTCTGCCTGTGCCTGCTCCTTGTCATACAGCCGCCAGATCC
GAGTGCAAGCGGAGCCATAAGTTTGTGCCTGGTGCTTGGCTTGCTGGCGAAGGCGTTGACGTGACA
AGCCTGAGAAGATCCGGCAGCTTCCCCGTGGACACCCAGAGATTTCTGAGGCCTGATGGCACATGC
ACCCTGTGCGAGAATGCCCTGCAAGAGGGAACACTGCAGAGACTGCCTCTGGCTCTGACCAATTGG
AGAGCCCAAGGCTCTGGCTGTCAGAGACACGTGACCAGAGCCAAGGTGTCCTCTACAGAGGCCGTG
GCTAGAGATGCCGCTCGGAGCATCAGAAACGACTGGAAAGTCGGCCTGGACGTGACCCCTAAGCCT
ACCAGCAATGTGCATGTGTCTGTGGCCGGAAGCCACAGCCAGGCCGCTAATTTTGCCGCTCAGAAA
ACCCACCAGGACCAGTACAGCTTCAGCACCGACACCGTGGAATGCCGGTTCTACAGCTTTCACGTG
GTGCACACACCTCCACTGCACCCCGATTTCAAGAGAGCCCTGGGAGATCTGCCCCACCACTTCAATG
CTAGCACACAGCCTGCCTACCTGAGACTGATCAGCAACTACGGCACCCACTTCATCAGAGCCGTGG
AACTCGGAGGCAGAATCTCTGCCCTGACAGCCCTGAGAACATGCGAACTGGCTCTGGAAGGCCTGA
CCGACAACGAGGTGGAAGATTGTCTGACCGTGGAAGCCCAAGTGAACATCGGCATCCACGGATCTA
TCTCTGCCGAGGCCAAGGCCTGCGAGGAAAAGAAAAAGAAACACAAGATGACCGCCAGCTTCCAC
CAGACCTACCGGGAAAGACACTCTGAGGTTGTCGGCGGCCACCACACCAGCATCAATGACCTGCTG
TTTGGCATCCAAGCTGGCCCTGAGCAGTACAGCGCTTGGGTTAACTCTCTGCCTGGCTCTCCTGGCC
TGGTGGATTACACACTGGAACCTCTGCACGTGCTGCTGGACTCTCAGGATCCTAGAAGAGAGGCTCT
GAGAAGGGCTCTGAGCCAGTACCTGACCGATAGAGCTAGATGGCGGGACTGCAGCAGACCTTGTCC
TCCTGGTAGACAGAAGTCCCCTAGAGATCCTTGCCAGTGCGTGTGTCACGGAAGCGCCGTTACCAC
ACAGGATTGCTGCCCAAGACAGAGAGGACTGGCCCAGCTGGAAGTGACCTTTATTCAGGCTTGGGG
CCTGTGGGGCGATTGGTTTACAGCCACAGATGCCTACGTGAAGCTGTTCTTTGGCGGCCAAGAGCTG
AGAACCAGCACCGTGTGGGACAACAACAACCCCATTTGGAGCGTGCGGCTGGATTTCGGAGATGTC
TTGCTTGCAACAGGCGGCCCTCTGAGACTGCAAGTGTGGGATCAAGACAGCGGCAGGGACGATGAT
CTGCTGGGCACATGTGATCAGGCCCCTAAGTCTGGAAGCCACGAAGTGCGGTGCAACCTGAATCAC
GGCCACCTGAAGTTCAGATACCACGCCAGATGTCTGCCTCACCTCGGCGGAGGCACATGTCTGGATT
ATGTGCCTCAGATGCTGCTCGGCGAGCCTCCTGGAAATAGAAGCGGAGCTGTGTGGTGA

Flexible Glycin-Serine linker, bold; T2A sequence, underlined.

Table S5. The nucleotide sequence of expression-optimized *UNC13D* exon 10.

GACTTGAGGTGTCGCGAAGATCAATGGTATCCTTTGGAGCCACGGACCGAAACTTATCCTGATCGC GGACAATGTCATCTTCAATTTCAGCTTATACACAAACGG

Table S6. Antibodies for flow cytometry and FACS

Antibody name	Clone	Vendor	Cat no.	RRID	Dilution or concentration
TruStain FcX™ (anti-mouse CD16/32)	93	BioLegend	101320	AB_1574975	5 µg/ml
Brilliant Violet 605™ anti-mouse CD19	6D5	BioLegend	115540	AB_2563067	1 µg/ml
Brilliant Violet 785™ anti-mouse/human CD45R/B220	RA3-6B2	BioLegend	103246	AB_2563256	1 µg/ml
APC anti-human CD2	TS1/8	BioLegend	309224	AB_2687219	1:200
PE anti-mouse CD62L	MEL-14	BioLegend	104408	AB_313095	1 µg/ml
APC anti-mouse/human CD44	IM7	BioLegend	103012	AB_312963	1 µg/ml
Brilliant Violet 785™ anti-mouse CD90.2 (Thy1.2)	30-H12	BioLegend	105331	AB_2562900	1 µg/ml
Brilliant Violet 650™ anti-mouse CD8a	53-6.7	BioLegend	100742	AB_2563056	1 µg/ml
FITC anti-mouse CD8a	53-6.7	BioLegend	100706	AB_312745	2.5 µg/ml
Brilliant Violet 785™ anti-human CD8	SK1	BioLegend	344740	AB_2566202	1:200
APC anti-human CD62L	DREG-56	BioLegend	304810	AB_314470	1:400
PE/Cyanine7 anti-human CD45RA	HI100	BioLegend	304126	AB_10708879	1:400
FITC anti-human CD95 (Fas)	DX2	BioLegend	305606	AB_314544	1:400
Brilliant Violet 421™ anti-human CD279 (PD-1)	NAT105	BioLegend	367422	AB_2721517	1:50
PE/Dazzle™ 594 anti-human TIGIT (VSTM3)	A15153G	BioLegend	372716	AB_2632931	1:100
PE anti-human CD366 (Tim-3)	F38-2E2	BioLegend	345006	AB_2116576	1:100
Brilliant Violet 711™ anti-human CD223 (LAG-3)	11C3C65	BioLegend	369319	AB_2716124	1:100
APC/Cyanine7 anti-human CD39	A1	BioLegend	328226	AB_2571981	1:100
Purified anti-mouse CD3ε	145-2C11	BioLegend	100301	AB_312666	10 µg/ml
Purified anti-mouse CD28	37.51	BioLegend	102101	AB_312866	5 µg/ml
PE anti-human Perforin	B-D48	BioLegend	353304	AB_2616860	1:50
Brilliant Violet 785™ anti-human CD8	SK1	BioLegend	344740	AB_2566202	1:200
PE anti-human CD107a (LAMP-1)	H4A3	BioLegend	328608	AB_1186040	1:200

Table S7. sgRNAs used for genome editing of mouse and human T cells.

Species	Name	Sequence (5′ → 3′)
Mouse	sgPrf1.1	GTACTTCGACGTGACGCTCA
Mouse	sgPrf1.2	CTGCCACGAAGCGTAAACAT
Mouse	sgB2m	CTGGTGCTTGTCTCACTGAC
Human	sgPRF1.1	GCGGGGGAGTGTGTACCACA
Human	sgPRF1.2	GGAGCTGGGTGGCCGCATAT
Human	sgUNC13D-ex10-mut	TCAGGACCTGCGCTGCTGAG
Human	sgB2M	GAGACATGTAAGCAGCATCA
Human	sgHBB.1 (Technical control)	CTTGCCCCACAGGGCAGTAA
Human	sgHBB.2 (Technical control)	TCCACTCCTGATGCTGTTAT

Table S8. Sequences of primers used in this study.

Species	Figure	Primer name	Sequence (5′ → 3′)
Mouse	Fig. 2E	Prf1.5HA.Fw	CCTCCTCTATGCATGAGCACTT
		Prf1.3HA.Rv	CCACATGATGGGTGGAGACAA
		Prf1.3HAintern.Rv	ATCCTGGCACTCACACTG
Mouse	fig. S1	B2m-5HA-For	GGACCTTCTGGTCTGAAGCA
		B2m-3HA-Rev1	CATGTGCACCTTGAAGCGC
		B2m-3HA-Rev2	CTGGCATGAAAGGCGTGAG
Human	Fig. 6	PRF1.5HA-Fw	GTGACCTTGAGCAGTCCTGA
		PRF1.3HA-Rv	gcaccatgtttgcccacaa
Human	Fig. 7	UNC13D.5HA-Fw	ACACAATGAAGGCCCACCTC
		UNC13D.3HA-Rv	AGGGCTGTGTACTCACGCCA
Human	fig. S2	B2M-5HA-For	CATGTAGACTCTTGAGTGATGTGTTAAGGAATGCTATGA
		B2M-3HA-Rev	ACTGGGCAGATCATCCACCTTCCTGATGCT
Human	fig. S6	i5Nextera-3′-GSP (−)	TCGTCGGCAGCGTCAGATGTGTATAAGAGACAGGTTTAATTGAGTTGTCATATGTTAATAACGGT
		i5Nextera-5′-GSP (+)	TCGTCGGCAGCGTCAGATGTGTATAAGAGACAGATACCGTTATTAACATATGACAACTCAATTAA
		i7Nextera-Rev	GTCTCGTGGGCTCGGAGATGTGTATAAG
		dsODN-For	5′- P-G*T*TTAATTGAGTTGTCATATGTTAATAACGGT*A*T -3′
		dsODN-Rev	5′- P-A*T*ACCGTTATTAACATATGACAACTCAATTAA*A*C -3′

Data S1. Genome-wide, unbiased off-target sites detected by GUIDE-seq. Detailed results corresponding to the experiments outlined in fig. S6 are given under three tabs (*PRF1*, sgRNA1 and 2; *UNC13D*, sgRNA1; *HBB* (technical control), sgRNA1 and 2). The R pipeline for processing and visualization of GUIDE-seq reads according to (*49, 73*) is available (*74*). Raw sequencing data have been submitted to NCBI SRA, accession PRJNA1016463. This table is supplied in Excel format (.xlsx) as a separate file.

Data S2. Tabulated data underlying Figs. 1 to 7, S1, S2, S4, S7, and tables S1 and S2.